Fronts and Cold Pools in the Oklahoma Mesonet: A 15-Year Climatology and Case Studies.

Andrew T. Lesage* and Steven K. Krueger

Department of Atmospheric Sciences, University of Utah, Salt Lake City, Utah

**Corresponding author address:* Andrew T. Lesage, Department of Atmospheric Sciences, 135 S 1460 E, Rm 819, Salt Lake City, Utah 84112-0110.

E-mail: andy.lesage@utah.edu

ABSTRACT

The Oklahoma Mesonet provides an extensive surface observation network for analyzing frontal passages and cold pools using station time series of temperature and pressure along with divergence on a triangular grid. These events were able to be further investigated in case studies and a 15-year climatology of frontal passages and cold pools. Cold pools extended around 50-100 km behind the front with duration primarily 30-60 mins under the algorithm used. Winter had the largest mean $-\Delta T$ and Δp (6.6 K and 2.9 mb) while spring and summer had the smallest magnitudes of $-\Delta T$ (5.8 K) and Δp (2.0 mb), respectively. Correlations between $-\Delta T$ and Δp were smallest in summer (0.15) and largest in winter (0.41). Surface convergence was similar in magnitude ahead of fronts from spring to fall while surface divergence behind fronts exhibited a distinct seasonal cycle; the largest values occurred during the summer and the smallest during winter. The magnitude of convergence ahead of fronts was not a strong indicator of cold pool formation. Fronts and cold pools were most frequent in June (3.8 fronts and 3.0 cold pools per triangle per June) while July and August had the highest percentage of fronts associated with cold pools. Fronts and cold pools were over twice as likely to occur during 21-0 UTC hours than during 1-19 UTC hours during the summer; other seasons showed a weak diurnal cycle with a slight nocturnal maximum.

1. Introduction

Cold pools are a prominent and common feature of frontal passages which have been studied for over half a century. Observations from the Thunderstorm Project described regions of descending air behind a squall line caused by evaporative cooling (Newton 1950). Convergence ahead of the leading edge of the cold pool with divergence behind was also noted as a prominent feature in case studies of these squall lines. The results were similar to those observed during the Cloud Physics Project in which pressure jumps, temperature falls, wind shifts, and precipitation features were observed with squall lines (Tepper 1950). Tepper referred to the squall lines as propagating "pressure jump lines".

In his synoptic analysis of squall lines in the Central United States, Fujita identified three main features of the associated surface pressure field: the pressure surge line, the thunderstorm high, and the wake depression (Fujita 1955). The pressure surge line marks the thunderstorms' leading edge and moves in the storm propagation direction. The thunderstorm high, later more commonly referred to as a mesohigh (Stout et al. 1957), is the high pressure region led by the pressure surge line that contains cool downdrafts that spread out upon reaching the surface. The region of surface cooling from these downdrafts is what would become known as the cold pool of the thunderstorm and is often associated with the mesohigh. The wake depression is a region of low pressure, typically behind the thunderstorm high, which forms a "pressure dipole" with the thunderstorm high.

Quantitative analysis of the dynamics and structure of a cold front in Oklahoma was first performed over half a century ago (Sanders 1955; Schultz 2008). Sanders found that horizontal temperature gradients and divergence associated with a cold frontal passage were strongest near the surface. Additionally, the cold front in Sanders (1955) progressed with a rearward tilt with height, which is most common though there are exceptions to this structure (Schultz and Steenburgh 1999). A model simulation revisiting the Sanders (1955) case found a vertical leading edge in the lowest km and a prefrontal wind shift (Schultz and Roebber 2008).

While the classical cold front conceptual model contains a colocated temperature decrease, pressure trough, and wind shift, this is far from the only type of cold front structure. Oftentimes these features are disconnected with a prefrontal trough or prefrontal wind shift ahead of the cold front (Schultz 2005). Schultz reviewed ten different mechanisms, six internal and four external, potentially responsible for prefrontal wind shifts. The magnitude of potential temperature gradients were larger for a case with coincident temperature gradient, pressure trough, and wind shift, than in a case with similar initial horizontal temperature gradient and frontogenesis but with a prefrontal wind shift (Schultz 2004).

In some cases a temperature increase is possible after a cold frontal passage (Doswell III and Haugland 2007). Their 7 December 2006 case involved a front where shear-induced turbulence from strong postfrontal winds resulted in mixing of a pre-frontal surface inversion which had developed overnight in calm winds.

Evaporation of convective precipitation has long been known to result in downdrafts (Humphreys 1914). Cold pool wakes have been shown to recover faster if the downdraft region contains weaker subsidence (Johnson and Nicholls 1983). When these downdrafts reach the surface they spread horizontally as density currents with divergent flow (Knupp and Cotton 1985; Knippertz et al. 2009). In studies where only surface variables are known, surface winds have been used to estimate downdraft mass fluxes (Sun and Krueger 2012).

Downdrafts have been found to cause damage through strong surface outflow winds (Fujita and Wakimoto 1981; Coleman and Knupp 2011). These outflow winds are gust fronts, "the leading edge of a mesoscale pressure dome followed by a surge of gusty winds on or near the ground"

(Wakimoto 1982). Wakimoto found that gust front edges were frequently the location of updrafts. The gust front propagation speed increases with the horizontal pressure gradient driving the gust front (Seigel and van den Heever 2012). High surface winds in the outflows are commonly found with slow propagation speeds, large amplitude pressure disturbances, and ambient winds of the same sign, such as a headwind with a pressure trough (Coleman and Knupp 2009).

Cold pools have a large range of sizes. Those associated with a single cumulonimbus cell are on the order of 10 km across (Tompkins 2001) while cold pools associated with a mesoscale convective system (MCS) can be 100-400 km wide (Stensrud et al. 1999). Air entrained from above the boundary layer into the wake of the downdraft resulted in temperature recovery of the cold pools in the Tompkins study.

A four-stage convective life cycle for MCSs was developed by Engerer et al. (2008) based on Oklahoma Mesonet cases that produced cold pools: 1) first storms, 2) MCS initiation, 3) mature MCS, and 4) MCS dissipation. The stages with the largest potential temperature decrease and pressure increase, respectively, were 9.5 K for the first storms stage and 4.5 mb for the mature stage. Adams-Selin and Johnson (2010) also used Oklahoma Mesonet data to find thirty-six bow echo cases and produced a conceptual model for bow echoes that exhibits a pressure rise and temperature drop pattern associated with cold pools.

Cold pool climatologies have been performed for the Atlas Mountains regions of North Africa (Emmel et al. 2010; Redl et al. 2015). For An Integrated Approach to the Efficient Management of Scarce Water Resources in West Africa (IMPETUS) data Emmel et al. (2010) used dew point temperature increases and wind speed thresholds for rain-free stations to identify density currents at stations. IR satellite images were examined manually to subjectively verify the presence of those identified density currents. Later work by Redl et al. (2015) used brightness temperature at microwave frequencies as an objective satellite verification method for cold pool leading edges.

In this study, temperature drops and pressure rises at Oklahoma Mesonet automated weather stations are analyzed for the 1997-2011 period to generate a dataset for a climatology. These time series are used with a triangular spatial grid. Fronts associated with convective, mesoscale, and synoptic systems would be detected in this front analysis. Cold pool area is defined to include regions of surface divergence exceeding a threshold following a frontal passage, which is detected by a temperature drop and a pressure rise.

Modeling studies have looked at downdraft and cold pool influences on convection. Colliding outflow boundaries have been modeled in 3-D numerical cloud models (Droegemeier and Wilhelmson 1985). It was found that collision areas were warmer and moister resulting in greater lifting of air over the cold pool aiding in the formation of new convection. Simulations of squall lines have shown that low-level shear can aid in deeper lifting at cold pool outflow boundaries allowing squall lines to maintain structure for several life cycles of convective cells (Rotunno et al. 1988).

Modeling of GATE ship array cases found that precipitation evaporation influences the wake height and thermodynamic characteristics (Nicholls and Johnson 1984). Without evaporative precipitation the mixed layer would be shallower with reduced surface fluxes due to a higher mixed layer temperature. Analysis of simulated trade wind cold pools from Rain In Cumulus over the Ocean (RICO) campaign data found updrafts close to the cold pool boundary were moister and had higher vertical velocity than updrafts further away from the cold pool (Li et al. 2014).

Parameterizations have looked at convective cells for years; however, convective downdrafts were considered to be a lesser source of downward mass flux compared to the environment and thus were left out (Moorthi and Suarez 1992; Pan and Randall 1998). Neglecting the compensating cumulus downdraft mass fluxes tends to result in a too warm and dry lower troposphere (Johnson

1976). Later versions of models included downdrafts as well as exchanges between clouds and the environment (Cheng and Arakawa 1997; Kain and Fritsch 1990).

One attempt at parameterizing cold pool processes involved parameterizing cold pool area, depth, and propagation speed, treating the propagation like a gravity wave that recovers via surface and entrainment fluxes (Qian et al. 1998). The scheme performed reasonably well for GATE, Tropical Ocean and Global Atmosphere Coupled Ocean-Atmosphere Response Experiment (TOGA-COARE) cases and when incorporated in the NCAR Community Climate Model (CCM3), albeit with shallow, warm, and moist biases (Rozbicki et al. 1999).

Another method of parameterizing cold pools involved a prognostic variable, *org*, which attempted to capture the effects of convective organization on properties of entraining plumes (Mapes and Neale 2011). A higher *org* value resulted in more entrainment, precipitation, convective heating, and rain evaporation.

Cloud-system resolving simulations with parameterized large-scale circulation have found that convection remains disorganized with weak vertical shear, but larger vertical shear resulted in linear mesoscale systems (Anber et al. 2014). They found that high surface fluxes had higher organization even without shear, suggesting that, while shear can promote organization, it is not required. The more organized systems had more rain, larger mass fluxes, more cloud cover, higher vertical velocity, and higher moist static energy.

Pressure rise data in this study could serve as a basis for comparison of rain evaporation estimates. Fujita proposed a method to estimate rain evaporation which assumed that the pressure rise is a result of cooling (and associated hydrostatic adjustment) due to precipitation evaporation (Fujita 1959). Comparing such rain evaporation estimates to rain evaporation derived from convection-resolving model simulations would allow one to test and refine the method. The resulting rain evaporation estimates could be used to evaluate and improve microphysical parameterizations in convection-resolving models. More accurately representing regions of cold air production due to precipitation evaporation and surface outflow boundaries could lead to an improved predictability of cold pool properties and convection initiation which could, in turn, be used to evaluate cold pool parameterizations in global weather and climate models.

2. Methodology

a. Oklahoma Mesonet dataset

The 1997-2011 period of Oklahoma Mesonet dataset was used in this analysis (Brock et al. 1995; McPherson et al. 2007). Mesonet observations have been collected since 1994 at 5-minute frequency with each county of Oklahoma represented by at least one station for a total of over 100 stations spaced “just under 30 km” apart (Engerer et al. 2008). The data were downloaded from the ARM archive (Atmospheric Radiation Measurement (ARM) Climate Research Facility 2012).

Mesonet stations were placed with preferences for rural sites with low-level vegetation, away from lakes and forests, on a slope less than 5°, with soil properties representing a large area, and that any obstructions should be at least 20 times the height of the obstruction away from the site (Brock et al. 1995). However, not all stations could meet all of the preferences due to variations primarily involving how hilly and forested terrain is across the state.

Mesonet site instrumentation, uncertainty, and resolution are detailed in Brock et al. (1995). A 10-m Rohn 20G tower holds a R. M. Young 5103 wind monitor mounted at 10m AGL for wind speed and direction and a modified Vaisala HMP35 sorption probe with a thermistor to measure relative humidity and temperature at 1.5m AGL. A Vaisala PTB 202 barometer is included in the data logging enclosure. Precipitation is measured with a MetOne 099M tipping-bucket rain gauge with a wind screen to reduce influence from the rain gauge being sited in open areas.

Over the years stations have been added but for the purposes of this analysis, only the 113 stations present at the beginning of 1997 were considered. Six stations residing in the Oklahoma Panhandle were excluded to leave a simpler map for tracking fronts in case studies. Of the remaining stations, each station was checked for data availability of 1.5-m air temperature, 10-m vector average wind magnitude, 10-m vector average wind direction, and station pressure. Only stations which exceeded 90% data availability for a given year were included in analysis for that year, which ranges from 99 to 104 stations, to minimize the influence of stations that were down for significant amounts of time.

The climatology developed in this analysis is of frontal passages and cold pools at gridded Mesonet triangles, described in the following subsections. The station spacing of the Oklahoma Mesonet is sufficient to resolve large MCS events and their associated cold pools over many triangles while smaller systems, such as a cold pool from an individual cumulonimbus cloud, might be missed in the Mesonet data. Events that cover large portions of Oklahoma will be counted for each triangle crossing in order to represent the proportion of times a larger system is responsible for a front and/or cold pool the average triangle experiences.

b. Mesonet grid

Mesonet stations which met the observation threshold described in section 2a for a year were gridded using the Delaunay triangulation procedure (Fig. 1) similar to that used in Sun and Krueger (2012). The triangles provide the highest resolution supported by the Oklahoma Mesonet. Additionally, frontal passages could be tracked across the Mesonet using the triangle edges to map estimated movement. Triangular grid cells were defined in order to calculate surface divergence (described in section 2c). The resulting grids for each year contained some low aspect ratio triangles[1] along the border which were removed. Two stations very close to each other located at approximately 35°N 98°W resulted in two low aspect ratio triangles which were also removed. The station coordinates (longitude, latitude, and altitude) changed in the case of a few stations which moved during the 15-year period (1997-2011). These stations were excluded from the grid during the year in which they moved. Due to the varying number of stations that met the observation threshold each year, and to stations that changed location during a year, the grid was adjusted slightly from year to year.

It was also determined that triangles with relatively long side lengths were not representative of the temporal scales used in the analysis of this study which require all three corners of a triangle to experience a frontal passage within two hours. After considering having a large enough maximum side length to retain most of the center of the grid, but small enough that triangles would not lose too many fronts due to speed requirements to cross the triangle, all triangles with a longest side length of greater than 80 km were excluded. This resulted in the removal of 10 to 13 triangles each year which were primarily along the borders of the domain.

c. Divergence

The Mesonet stations' 5-minute average wind magnitude and direction values were used to determine the divergence in each Mesonet triangle. This calculation used the equations for the horizontal divergence of triangles on irregular grids (Davies-Jones 1993; Dubois and Spencer 2005). Sun and Krueger (2012) performed these divergence calculations for the Oklahoma Mesonet specifically for surface divergence analyses. The divergence values then had a 15-minute rolling average applied to smooth out some of the noise in the data.

[1] The aspect ratio of a triangle is defined as $2R_i/R_o$ where R_i is the radius of the circle inscribed within a triangle and R_o is the radius of the circle circumscribed around the triangle.

d. Front analysis

Temperatures at each station were adjusted to remove the diurnal cycle. Without the removal of the diurnal cycle for temperature, many spurious frontal passages would be generated by the analysis in the late afternoon and evening when the surface is rapidly cooling. The diurnal cycle for a station was calculated based on the average temperature for each observation time. The average temperature was determined by using all valid temperature measurements at a station during the 15-year period for the observation time as well as all of the observations 24 and 48 hours before and after the observation time at the station (Eq. 1).

$$T_{\text{diur.}} = [\sum_{1997}^{2011} \sum_{\text{day}-2}^{\text{day}+2} T_t]/n \tag{1}$$

In this equation, n is the total number of valid observations and t is the observation time. Though much less likely to cause a spurious front detection, the diurnal cycle was also calculated for the pressure observations. These diurnal temperature and pressure values were then subtracted from the observations to yield the diurnal cycle adjusted datasets of temperature and pressure.

Since temperature drops and pressure rises comprise the core aspects of cold frontal passages, and frontal passages sometimes involve one much more than the other, combining these two variables provides a useful metric for front occurrence and strength. The front score (FS) is a unitless variable used in this study to represent the strength of a frontal passage. The FS uses the diurnal-adjusted over 30-minute interval temperature falls, $-(\Delta T)_{30}$, and pressure rises, $(\Delta p)_{30}$, calculated every 5 minutes. For example, the FS at 1230 UTC uses the changes in adjusted temperature and pressure between 1200 UTC and 1230 UTC. A 1 mb pressure increase is equivalent to a 1 K temperature drop. Later, observations will show that temperature drops tend to be larger than pressure rises. Adding these changes yields the FS:

$$\text{FS}(t) = -1\ \text{K}^{-1}(\Delta T)_{30} + 1\ \text{mb}^{-1}(\Delta p)_{30}. \tag{2}$$

As an example, the FSs at the Blackwell Mesonet station for JJA 1997 are shown in Fig. 2. The front scores for all stations for all 5-minute observations over the 1997-2011 period are shown in Fig. 3. Higher magnitude positive front scores are more common than negative front scores of the same magnitude.

FSs were used to detect when a frontal passage occurred at a Mesonet station or triangle. A front is considered to have reached a Mesonet station when (1) the FS at the station exceeds a threshold and (2) the FS is the maximum value reached during the 6 hours centered at the analysis time. Requiring both conditions more accurately identifies the primary front associated with a system. A FS $>=$ 3 was used as the threshold to detect a front.

A frontal passage at a Mesonet triangle (as opposed to a Mesonet station) is stipulated to have occurred if all three stations that comprise the triangle corners experience a frontal passage within a 2-hour interval. The 2-hour limit limited the size of triangle side length that could be used so as to avoid an underestimate in frontal passage frequency. However, extending the 2-hour limit would have captured more spurious fronts. The duration of a frontal passage at a triangle is the time elapsed from when the first corner is reached until the time when the last corner is reached. The resulting fronts could be tracked across the Mesonet as they progressed through Oklahoma.

The statistics of changes in temperature and pressure were comprised of all three corner stations of the triangle individually involved in a frontal passage across a Mesonet triangle. The maximum temperature drop during a frontal passage, $-\Delta T$, was calculated by subtracting the lowest temperature within 2 hours after the frontal passage at a station from the highest temperature within 30 minutes before the frontal passage. The maximum pressure rise, Δp, was calculated by subtracting the lowest pressure within 30 minutes before the frontal passage at a station from the highest pressure within 2 hours after the frontal passage. This finds the total changes in pressure or temperature associated with a front while $-(\Delta T)_{30}$ and $(\Delta p)_{30}$ were used to ensure that the temperature decreases and pressure increases are connected.

e. Cold pool analysis

Surface divergence is used in this study to separate fronts associated with cold pools from other frontal passages. Consequently, *a cold pool region is defined in this study to be a Mesonet triangle with surface divergence (that exceeds a threshold described below) following a frontal passage.*

The cold pools in this study generally consist of regions in which a cold air mass is expanding via precipitation processes such as evaporative cooling and downdrafts. Precipitation is necessary for evaporative cooling, though the precipitation does not have to reach the ground for evaporative cooling to occur. Dry (non-precipitating) frontal passages generally did not result in cold pools in this study due to insufficiently large divergence values.

Quantitatively, a cold pool was deemed to have occurred in this study at a Mesonet triangle if the triangle experienced a frontal passage and if the 15-minute-averaged strong divergence threshold ($10^{-4}\mathrm{s}^{-1}$) was exceeded within half an hour before to an hour after the front propagates halfway through the triangle. The longer time duration after the frontal passage recognizes that cold pools follow gust fronts. It is possible, given the resolution of the Mesonet grid, that a cold pool region could seemingly be slightly ahead of a front. When a cold pool region is determined to have occurred, its duration at the triangle is calculated. The time interval during which the divergence exceeds half of its maximum value in a triangle is defined as the stations' cold pool duration. The half maximum is used to reduce the influence of triangle size on divergence. Other studies with three-dimensional data have used near-surface negative buoyancy thresholds to identify cold pools (Tompkins 2001; Feng et al. 2015). For the Mesonet, divergence at the surface is the closest analogue to negative buoyancy.

Fig. 4a shows the average precipitation for each divergence bin with precipitation rates higher for higher magnitude divergence values, and higher for divergence than convergence. Fig. 4b shows that the percentage of fronts with precipitation is approximately 50% for the divergence threshold used in this study and exceeds 80% for maximum divergence values above double the threshold. This result indicates that high divergence is indicative of precipitation which is commonly associated with cold pools.

3. Case study results

Identified fronts and cold pools can be tracked across the Mesonet giving a detailed view of the analysis for case studies. Over the course of 15 yrs of Mesonet data, tens of thousands of frontal passages at triangles were detected in the Oklahoma Mesonet. Hundreds of events involving a front that sweeps through large portions of the Mesonet can be used for case studies. Four such cases will be shown in this section: 1) 13 June 1997, 2) 15-16 June 2002, 3) 30 April 2011, and 4) 24-25 May 2011. These cases are supplemented with radar images from the UCAR image archive.

a. 13 June 1997 case

At approximately 0000 UTC on 13 June 1997 a squall line, which initiated in southeastern Colorado and northeastern New Mexico, entered Kansas, the Oklahoma Panhandle, and Texas. The disorganized line of thunderstorms reached the Mesonet grid at roughly 0300 UTC and was tracked for the next seven hrs across the Mesonet (Fig. 5) with isolated thunderstorms popping up ahead of the main line. At 0330 UTC (Fig. 5a) the front analysis found only smaller segments of a front in western and northwestern portions of Oklahoma. The radar images show a gap between two thunderstorms that coincides with the lack of strong convergence (Fig. 5a). In the areas where a front was defined, convergence was present to the east ahead of the front and divergence to the west behind the front. At 0330 UTC there was only one triangle designated as in a cold pool, located in the northwestern corner of the Mesonet domain.

From the 0500 UTC front analysis (Fig. 5b), the stronger, more well-defined front marked the leading edge of the system which had been organizing over the previous two hours. There was some bowing of the front present with trailing stratiform precipitation. The squall line had caught up to the isolated thunderstorms that developed ahead of the line. The area ahead of the front had strong convergence while strong divergence was present behind the front. Farther behind the front, near the back edge of the stratiform precipitation, there was a second region of convergence where a one-triangle front is marked. The analysis was designed to capture the strongest fronts at each triangle and in this instance this latter front was stronger at that particular triangle than when the initial line passed through. This was likely a result of the squall line being somewhat disorganized in that area at the time it passed that triangle. A large active cold pool stretched from the front of the main squall line to the back edge of the stratiform precipitation in western Oklahoma.

From 0500 to 0700 UTC, a supercell at the south end of the squall line separated from the rest of the line. This separation is shown in the form of a gap in the front indicated by lower FSs and the lack of significant radar returns (Fig. 5c). The southern cell had weaker FSs than the more well defined squall line to the northeast. The region of strong divergence was primarily concentrated in northern Oklahoma, with a smaller area of strong divergence behind the southern supercell. Cold pools were identified in both of these areas. In western Oklahoma a few small convective cells had formed behind the secondary convergence line.

By 0900 UTC the southern supercell had progressed southeastward much farther away from the rest of the line while the main squall line continued eastward (Fig. 5d). The area of strong divergence behind the front was more concentrated on the southern half of the squall line. There was a weaker front to the east of the southern supercell. Behind the supercell to the northwest, trailing convection developed over the previous two hrs and eventually merges with the southern supercell (not pictured). There was clear separation between the convergence and divergence regions in the trailing convection. Overall, the front analysis performed well at representing the location of the front that would be expected based on the radar images. Despite the separation in the front, the cold pool along the front almost extended from the southern border with Texas to the northern border with Kansas. At this time, the primary cold pool has been in place for hours and has advanced eastward over time behind the squall line. However, large areas of stratiform precipitation were not classified as in a cold pool because the divergence values were not high enough at 0900 UTC. Many of the triangles in northeastern Oklahoma would likely be defined as in a cold pool using a different definition relying more on sustained stratiform precipitation or lingering temperature falls.

b. 15-16 June 2002 case

Around 1800 UTC 15 June, a line of thunderstorms oriented from northwest to southeast was located in northern Kansas and southern Nebraska moving southeastward. Over the next few hours the line merged with pop-up thunderstorms in western Kansas and spread out allowing for a much more southwest to northeast oriented storm front to develop as the combined system moved south towards the Oklahoma border. The frontal passage and cold pool (Fig. 6) analysis for this event are shown.

At 0000 UTC 16 June the squall line had just entered the northwest corner of Oklahoma. Very strong convection was present ahead of the line, including triangles over 50 km ahead of the squall line (Fig. 6a). Divergence behind the front was present as well since this line had developed into a mature system several hours earlier. The FSs exceeded the strong front threshold. A few isolated triangles along and just behind the line were designated as cold pools at this time.

Ninety minutes later the squall line had progressed further into the state reaching from almost the southwest corner to the northeast corner of Oklahoma (Fig. 6b). The stronger radar echoes were in the western half of the squall line, matching up with the stronger FSs. Additionally, the convergence-divergence pattern ahead of and behind the front was more well-defined in the western half of the state though present throughout the squall line. A broad region of heavy stratiform precipitation was located in northern Oklahoma. In that stratiform precipitation region a cold pool was detected far behind the squall line. Additionally, along the front there was a narrow band of scattered triangles that are in cold pool status, just behind strong convective cells.

By 0300 UTC the eastern half of the squall line had lost much of its strong convection resulting in a front that does not extend all the way to the Arkansas border (Fig. 6c) with regard to the FS threshold. The southwestern corner of Oklahoma still featured strong convection, with the line extended towards north central Texas. The eastern half of the state had lost most of its divergence behind the line as the convective structure had fallen apart. However, there was still a narrow region of convergence ahead of the squall line. South central Oklahoma had a very large area of divergence behind the front. This extended up into north central Oklahoma with the trailing portion of the stratiform precipitation region. A small line of convergence was detected in the stratiform precipitation region in north central Oklahoma with an additional larger line of convergence behind the stratiform precipitation. There were many triangles experiencing a cold pool in south central Oklahoma behind the squall line. Extending back several triangles deep, this cold pool covered roughly one eighth of the state. The eastern half of the state had much less cold pool coverage in this analysis though a couple triangles in the northeast corner were still in a cold pool where the front had passed over an hour prior.

As the system moved farther southeast the strength of the convection in Oklahoma weakened further as the strongest cells moved into Texas. The stratiform region of precipitation was well-defined and contained a large area of divergence behind the remnants of the squall line in Oklahoma (Fig. 6d). The line of convergence that was just behind the stratiform precipitation region had fallen farther behind the precipitation though it maintains an almost continuous line through a large portion of the northwest to north central region. The cold pool was concentrated in the south central stratiform precipitation with a few solitary triangles elsewhere in cold pools.

c. 30 April 2011 case

An example of a dry frontal passage is shown for a 30 April 2011 case (Fig. 7). At 0700 UTC (Fig. 7a) a strong front entered the northwestern corner of Oklahoma with a long line of strong convergence values ahead of it. As the front progressed across the state (Fig. 7b) the convergence ahead of the front remains with some of the line being detectable in the radar (as a narrow line of brighter green reaching from Iowa down into Texas at 0900 UTC). Divergence behind the front is very weak with no cold pools marked at this time. There is no precipitation anywhere in the state during the duration of this frontal passage.

Throughout the morning the line continues to cross Oklahoma. Every so often an isolated triangle will reach the divergence threshold and be marked as a cold pool, as was the case for 3 triangles still marked as such in Fig. 7c. The front strength weakens by mid-morning with a smaller length designated as a front (Fig 7d). However, by the afternoon showers and thunderstorms develop ahead of the front in Arkansas and southeastern Oklahoma (not shown).

d. 24-25 May 2011 case

The final case study is a case which occurred during the Midlatitude Continental Convective Clouds Experiment (MC3E). On 24 May the 1800 UTC sounding (not shown, UCAR archive) from Norman, Oklahoma (KOUN) had strong southerly winds at low-levels veering with height.

A strong stable layer at roughly 825 mb was in place; however, low-level moisture and unstable mid-levels resulted in CAPE values over 2500 Jkg^{-1}. The Storm Prediction Center (SPC) had issued a high risk convective outlook for central and northeastern Oklahoma.

By 2000 UTC the first thunderstorm cells had formed, rapidly developing into severe thunderstorms with a threat of tornadoes. The frontal passage and cold pool (Fig. 8) analysis had some difficulty capturing the front and any associated cold pool with these thunderstorms due to the low resolution of the Mesonet station grid (Fig. 8a). There was a large region of convergence both ahead of and behind the supercells at this time. The front, although strong, did not extend throughout all of the supercells, and only one triangle observed a cold pool at this time.

Over the next couple hrs, more cells had flared up and a clear north-south line had formed (Fig. 8b) though there were gaps between the cells that made up the line. There was only a slight signature of the usual convergence-divergence pattern ahead of and behind the front, possibly a result of the strong rotation in tornadoes, or systems capable of potentially producing tornadoes. At this point multiple tornadoes had formed, including one that struck the El Reno Mesonet station at 2120 UTC recording a maximum wind gust of 151 mph. Only a few triangles in north central and northwestern Oklahoma observed cold pools at the time. Strong rotation tends to lead to surface inflow from all directions, reducing the likelihood of divergence and cold pools behind a front in this situation.

By 0000 UTC, however, the squall line was straighter and had fewer, smaller gaps between individual storm cells (Fig. 8c). A convergence-divergence distribution ahead of and behind the front was more well-defined in the north central Oklahoma line than the smaller, weaker (in terms of front strength) line in south central Oklahoma. A large region of convergence is present in northwestern Oklahoma where a secondary front was present that lacked precipitation. Cold pool coverage had grown behind the main line in central Oklahoma.

As the main front progressed further eastward the strength of the front weakened slightly with regards to FSs (Fig. 8d). However, convection was still intense with radar echoes reaching up to 60 dBZ. The fronts in western Oklahoma had a disorganized structure and covered more area at this time. Cold pools were detected behind the main storm line. Radar coverage in northwestern Oklahoma was sparse by comparison, though the secondary line does not appear to develop precipitation as it moves throughout the state the next few hours. At 0300 UTC (not shown) there was a faint green line visible on the radar signifying this secondary front.

e. Cold pool time series

Observing the change in cold pool area over time allows for greater visualization of the size and time scales of the areas experiencing a cold pool (Fig. 9).

From roughly 0300 to 1100 UTC in the 13 June 1997 case at least one Mesonet triangle resided in a cold pool (Fig. 9a). The peak size of cold pool area was around 0930 UTC at a size of nearly 14×10^3 km^2. Around a third of the cold pool areas retained a cold pool for at least 30 mins, and some triangles, particularly later in the period, retained cold pool status for over an hr.

For the 15-16 June 2002 case the cold pool time series shows a larger maximum cold pool area than the first case study with a maximum size of roughly 18×10^3 km^2 (Fig. 9b). The duration of the cold pools tended to be longer than the first case study. Later in the time period over half the cold pool area comprised of locations which had been in a cold pool for half an hr or more. The cold pool area that was present for at least an hr peaked at roughly 5×10^3 km^2 around 0400 UTC.

For the 30 April 2011 dry frontal passage case the cold pool time series showed very little cold pool coverage with a maximum that only reached roughly 2.5×10^3 km^2 (Fig. 9c). There are frequent jumps in the amount of area covered by cold pools.

The cold pool time series for the final case study showed a maximum cold pool area of just over 11×10^3 km^2 (Fig. 9d). The entire period with cold pools present lasted approximately 10 hrs. The cold pools were rather short in duration with few lasting even half an hr. Cold pools later in the event had longer durations than cold pools in the first half of the event, a result likely due to the increased organization of the convergence-divergence gradient across the front over time.

f. Front characteristics

For each of the four case studies the average divergence, temperature, and pressure timeseries were identified and centered on the time step when the front was halfway through the Mesonet triangle. For temperature and pressure each triangle uses the average of the three corner Mesonet stations. The average time series is plotted along with the standard deviation for each variable and case (Fig. 10). For temperature and pressure, the values are normalized to 0 at the midpoint of frontal passage. As a result, the standard deviation near the midpoint was artificially low so the standard deviations for temperature and pressure 15 minutes before and after the frontal passage midpoint are removed. The x-axis was reversed on the plot to show a west to east pattern.

For the fronts with precipitation the divergence profile begins in similar fashion with a dip towards strong convergence values before a reversal to strong divergence as the front crosses the triangle. However, for two of the cases the average divergence trends back towards 0 after the frontal passage while for the 15-16 June 2002 case the average divergence remains at an elevated level even two hours after the middle of frontal passage. The dry frontal passage starts like the others with strong convergence but instead of strong divergence behind the front it merely returns to around 0.

Temperature profiles start similarly with temperatures around 3-4 K higher on average before frontal passage than in the middle of a frontal passage. The drop in temperature begins around 30-

45 minutes before the middle of a frontal passage and continues until around 15 minutes afterwards generally. After frontal passage three of the cases show a slight rebound in temperature of 1-2 K. The dry frontal passage case has the largest temperature drop and continues falling long after the front has passed.

Pressure profiles start with a wide range of lower pressure values before frontal passage but show an increasing trend during frontal passage. For the 13 June 1997 and 15-16 June 2002 cases there is a drop off in pressure after frontal passage, while for the 24-25 May 2011 case the average pressure drop after frontal passage is minimal. For the 30 April case pressure continues to increase after the front.

g. Front wind maps

Using the front locations from the case studies plots of front propagation speed can be made for the case studies (Fig. 11) and (Fig. 12). These plots help identify characteristics of the front such as the separation in the 13 June 1997 case where the main storm line propagates to the east southeast while the southern supercell moves more southward at a slower speed (Fig. 11a). Propagation speeds are roughly a factor of 2 different in that instance. Generally, front speeds are similar in adjacent triangles with the five minute time resolution being a contributor to the differences.

The 15-16 June 2002 case shows near uniform south to southeast flow through Oklahoma with wind speeds primarily around 20 ms^{-1} (Fig. 11b). An exception is around 0400 UTC when most triangles experiencing a front are closer to 10-15 ms^{-1}. Around this time the primary area of strong convection was in southwestern Oklahoma which ended up surging farther ahead of the stratiform precipitation regions to the east where the front speed appears to slow.

The dry frontal passage 30 April 2011 case developed northwest of Oklahoma and swept across the state (Fig. 12a). The speed of the front decreased over time until eventually weakening in eastern Oklahoma during mid-morning.

In the 24-25 May 2011 case the front speed is generally 10-15 ms^{-1} across Oklahoma (Fig. 12b). The front itself propagates east-southeastward though the storm cells that make up the line move from the southwest to northeast.

4. 15-year climatology of fronts and cold pools

The 1997-2011 period of Oklahoma Mesonet data was analyzed for frontal passages (across Mesonet triangles) and cold pools and statistics were compiled. These frontal passage and cold pool statistics are now presented for: (1) temperature and pressure changes, (2) convergence/divergence, (3) monthly distribution, and (4) diurnal distribution.

a. Temperature and pressure changes

The seasonal average temperature and pressure changes during all frontal passages (FS 3+) are shown in Fig. 13. Seasons are defined as: spring (MAM), summer (JJA), fall (SON), and winter (DJF). Results for all frontal passages were similar to those for fronts associated with cold pools (not shown). Average temperature drops during frontal passages were smallest in spring (5.8 K) and largest in winter (6.6 K). Average pressure rises were smallest in summer (2.0 mb) and largest in winter (2.9 mb).

In comparison to Fig. 13, Engerer et al. (2008) found that the average pressure rise in cold pools from 39 MCS events between April and August was 4.5 mb (which occurred during the mature stage) while the average potential temperature fall was 9.5 K (which occurred during the first storms stage), likely a result of having a stronger set of cases than the climatology includes though the differences in methodology may also play a role. Additionally, the Mesonet dataset includes frontal passages at triangles which may only see one stage of the MCS or just a fraction of an MCS.

For individual stations, a frontal passage typically exhibited a 3 to 9 K temperature drop and a 0 to 4 mb pressure rise (Fig. 14). The correlation between $-\Delta T$ and Δp was low (0.28). Correlations were calculated for all fronts and strong fronts for each season (Fig. 15). Considering only fronts associated with cold pools made little change in the correlations (not shown). Summer correlations were the smallest in magnitude while winter and spring had the largest correlations.

The correlations of $-\Delta T$ with Δp varied from 0.41 for fronts during the winter to only 0.15 for fronts during the summer. Engerer et al. (2008) also reported a weak to moderate correlation (0.38) between $-\Delta T$ with Δp. Engerer et al. (2008) speculated that the weak relationship between $-\Delta T$ and Δp is due to the complex vertical buoyancy profiles that often occur within and above cold pools (Bryan et al. 2005). As a consequence, the surface temperature deficit is often not correlated with the buoyancy profile and the resulting surface pressure rise. This relationship between $-\Delta T$ and Δp may at least partially explain the low correlations found during the summer, which was when the largest fraction of fronts were associated with cold pools (detailed in section 4c).

b. Convergence/divergence

Divergence values were calculated for the beginning, middle, and end of each triangles' frontal passages. The beginning of the frontal passage was defined as the observation time when the first corner of a Mesonet triangle experiences a local maximum FS. The end of the frontal passage was defined as the observation time when the third corner of a Mesonet triangle experiences a local maximum FS. The middle of the frontal passage was the observation time halfway between the beginning and the end.

The average divergence values for all frontal passages are shown (Fig. 16a). On average, as a front reaches a Mesonet triangle, there is strong convergence (divergence $< -10^{-4}$ s^{-1}). The magnitude of the convergence at the beginning varied slightly from season to season with convergence for all fronts slightly weaker in winter and convergence for strong fronts slightly stronger in spring and fall. Halfway through the frontal passages, there were large seasonal differences in divergence. Summer frontal passages had divergence on average while the other three seasons maintained convergence. At the end of a frontal passage, summer had the strongest divergence on average: a factor of 2 larger than spring and fall, and a factor of 5 larger than winter. End-of-front divergence in summer was roughly the same magnitude as beginning-of-front convergence. For the other three seasons the magnitude of convergence at the beginning of a frontal passage was 2 to 5 times the magnitude of divergence at the end of a frontal passage.

Average divergence values for frontal passages that produced cold pools are also shown (Fig. 16b). Because cold pools required the divergence threshold to be exceeded, their ending divergence and mid-passage divergence values were larger than for all frontal passages. However, the seasonal pattern was about the same as for frontal passages with summer having the highest divergence values for the middle and end of frontal passages and winter having the lowest convergence at the beginning of frontal passages and lowest divergence at the end of frontal passages. It is notable that the beginning covergence values were roughly the same for cold pools as for all frontal passages. This suggests that the strength of convergence ahead of a front is not closely related to the strength of divergence behind a front.

c. Monthly distributions

For the monthly distributions, the data from the triangles which experienced fronts or cold pools were used (Fig. 17). There were more fronts (3.8 per triangle per month) and cold pools (3.0

per triangle per month) during June than the other months. December had the fewest fronts and January the fewest cold pools. The higher frequency of fronts from April-June matches up well with the time of the annual maximum of convective activity in Oklahoma. Frontal passages during July and August had the highest percentage of fronts associated with cold pools.

d. Diurnal distributions

The mean diurnal distributions of frontal passages and cold pools were calculated by summing the number of fronts and cold pools present in all triangles for each hourly interval (0000-0055 UTC, 0100-0155 UTC,..., 2300-2355 UTC) during each season for the 15-year period of record (1997–2011) (Fig. 18). The error bars indicate the standard deviations of the yearly means.

There was a significant seasonal variation in the diurnal distribution of frontal passages. In the summer (Figure 18b) there was a large peak in frontal passage frequency in the afternoon, from 20-01 UTC (14-19 LST), with frontal passage frequencies then twice as high as during the rest of the day. The other three seasons exhibited relatively small amplitudes in their diurnal cycles. The diurnal distribution of cold pool frequency (not shown) was very similar to that for frontal passages.

The percentages of frontal passages with cold pools were also calculated for the diurnal cycle (Fig. 19). In spring, roughly 60% of fronts are associated with cold pools throughout most of the day. The morning hours were the exception with the percentage dropping below 50% for several hours (15-19 UTC). Summer had the largest fraction of frontal passages associated with cold pools, exceeding 80% in the evening hours. No individual hour during summer fell below 70%. In the fall evening hours approximately 60% of frontal passages are associated with cold pools. During the day these percentages fell to between 40 and 50% until the mid-afternoon. In the winter the fraction of frontal passages associated with cold pools was between 30 and 40%

except for a few hours in the evening which dropped lower. Winter fractions were approximately half as large as summer.

5. Conclusions

A 15-year climatology of Oklahoma Mesonet frontal passages and cold pools was created and analyzed. Previous studies involving cold pools in the Oklahoma Mesonet have looked at shorter time periods with a focus on features such as MCSs (Engerer et al. 2008), squall lines (Adams-Selin and Johnson 2010; Hocker and Basara 2008a), and supercells (Hocker and Basara 2008b).

Additionally, four cases studies were analyzed representing a very small fraction of the 15 yrs of Mesonet data. However, they highlight varying storm structures and profiles of key variables. The 13 June 1997 and 15-16 June 2002 cases involve MCSs tracking through the Mesonet with a strong forward line of thunderstorms with a large region of trailing stratiform precipitation. The 30 April 2011 case showed an example of a dry frontal passage which showed a lack of strong divergence when precipitation was not present. The 24-25 May 2011 case involved supercells which formed into a line crossing Oklahoma, with more rotation which likely resulted in the delayed formation of a convergence-divergence couplet in the storm line.

The cold pools in this study were similar to other studies in terms of length along a front. However, the width a cold pool extended behind the lead storm axis was typically only 50-100km in these cases while the distances can be 100-400 km for other analysis techniques (Stensrud et al. 1999). Most triangles in the Mesonet case studies remained in cold pools for 30-60 mins.

The temperature falls and pressure rises during frontal passages were objectively determined. Spring had the smallest average temperature falls while summer had the smallest average pressure rises. Both variables had their largest average magnitude changes in the winter. Correlations between $-\Delta T$ and Δp for individual frontal passages were low, 0.28, with the smallest correlation in summer and highest in winter and spring. The average temperature and pressure changes and their correlations were generally similar for all fronts and fronts associated with cold pools. Since the Mesonet observations are at the surface, obtaining vertical profiles of temperature could improve understanding of the reasons for the low correlations between changes in pressure and temperature during frontal passages, particularly in the summer.

Cold pools were evaluated based on temperature falls, pressure rises, and surface divergence. The associated gust front exhibits convergence ahead of the front and divergence behind the front. Convergence values ahead of frontal passages were similar from spring to fall with slightly lower values in winter. However, summer frontal passages transitioned to divergence sooner, and had larger divergence values as a front finished crossing a Mesonet triangle, than was the case for the other seasons, especially winter. While divergence values were much stronger for fronts resulting in cold pools than all fronts because of the divergence requirement, the convergence values ahead of a front showed very little difference between all fronts and fronts resulting in cold pools.

June had the highest frequency of cold pools while July and August had the highest percentage of frontal passages which resulted in cold pools. Winter months were the lowest in all three categories. In contrast, May was the most frequent month for squall lines and supercells over Oklahoma in 1994-2003 climatologies (Hocker and Basara 2008a,b). August had the highest number of density currents and cold pools in studies of the Atlas Mountains (Emmel et al. 2010; Redl et al. 2015).

The diurnal cycle of fronts and cold pools showed a strong seasonal variation. During the summer, frontal passages and cold pools were most frequent in the late afternoon to evening hours, coinciding with daytime-heating-induced convection, over twice as often as the other hours ($\sim$130 vs $\sim$50 per summer). The other seasons had much smaller diurnal variation in frontal passage and cold pool frequency. The summer pattern was the dominant influence on the annual pattern for the diurnal cycle. In Hocker and Basara (2008b) supercell initiation was most frequent in the late afternoon while in Hocker and Basara (2008a) squall line initiation was most frequent in the early evening hours.

The methods used in this analysis could be applied to simulations using convection-resolving models such as the Weather Research and Forecasting (WRF) model and the System for Atmospheric Modeling (SAM). Particularly useful would be increased resolution in a model relative to that of the Oklahoma Mesonet. Higher resolution would improve the sampling, especially for cases of smaller-scale features and isolated convection that can be missed by the 40-km spacing of the Mesonet stations. A regularly spaced grid in a model simulation would allow for evaluating geographic distributions.

Acknowledgments. This research was supported by the Office of Science (BER), U.S. Department of Energy, Grant No. DE-FG02-08ER64553. Data were obtained from the Atmospheric Radiation Measurement (ARM) Program sponsored by the U.S. Department of Energy, Office of Science, Office of Biological and Environmental Research, Climate and Environmental Sciences Division. Oklahoma Mesonet data are from a cooperative venture between Oklahoma State University and The University of Oklahoma, supported by the taxpayers of Oklahoma. Radar images are obtained from the University Corporation for Atmospheric Research (UCAR) image archive.

References

Adams-Selin, R. D., and R. H. Johnson, 2010: Mesoscale surface pressure and temperature features associated with bow echoes. *Mon. Wea. Rev.*, **138**, 212–227, doi:10.1175/2009MWR2892.1.

Anber, U., S. Wang, and A. Sobel, 2014: Response of atmospheric convection to vertical wind shear: Cloud-system-resolving simulations with parameterized large-scale circulation. Part I: Specified radiative cooling. *J. Atmos. Sci.*, **71**, 2976–2993, doi:10.1175/JAS-D-13-0320.1.

Atmospheric Radiation Measurement (ARM) Climate Research Facility, 2012: Oklahoma Mesonet (05OKM). 1997-01-01 to 2011-12-31. Southern Great Plains (SGP) External Data (satellites and others) (X1), Compiled by: Atmospheric Radiation Measurement (ARM) Climate Research Facility Data Archive: Oak Ridge, Tennessee, USA. Data set accessed 2012-02-06., www.arm.gov/data/datastreams/05okm.

Brock, F. V., K. C. Crawford, R. L. Elliott, G. W. Cuperus, S. J. Stadler, H. L. Johnson, and M. D. Eilts, 1995: The Oklahoma Mesonet: A technical overview. *J. Atmos. Oceanic. Technol.*, **12**, 5–19, doi:10.1175/1520-0426(1995)012⟨0005:TOMATO⟩2.0.CO;2.

Bryan, G. H., D. Ahijevych, C. Davis, S. Trier, and M. Weisman, 2005: Observations of cold pool properties in mesoscale convective systems during BAMEX. *Preprints, 11th Conf. on Mesoscale Processes*, Albuquerque, NM, Amer. Meteor. Soc., JP5J.12. [Available online at http://ams.confex.com/ams/pdfpapers/96718.pdf.].

Cheng, M.-D., and A. Arakawa, 1997: Inclusion of rainwater budget and convective downdrafts in the Arakawa-Schubert cumulus parameterization. *J. Atmos. Sci.*, **54**, 1359–1378, doi:10.1175/1520-0469(1997)054⟨1359:IORBAC⟩2.0.CO;2.

Coleman, T. A., and K. R. Knupp, 2009: Factors affecting surface wind speeds in gravity waves and wake lows. *Wea. Forecasting*, **24**, 1664–1679, doi:10.1175/2009WAF2222248.1.

Coleman, T. A., and K. R. Knupp, 2011: A review of three significant wake lows over Alabama and Georgia. *Wea. Forecasting*, **26**, 766–773, doi:10.1175/WAF-D-11-00021.1.

Davies-Jones, R., 1993: Useful formulas for computing divergence, vorticity, and their errors from three or more stations. *Mon. Wea. Rev.*, **121**, 1449–1458, doi:10.1175/1520-0493(1993)121⟨0713:UFFCDV⟩2.0.CO;2.

Doswell III, C. A., and M. J. Haugland, 2007: A comparison of two cold fronts – Effects of the planetary boundary layer on the mesoscale. *Electronic J. Severe Storms Meteor.*, **2**, 1–12. [Available online at http://www.ejssm.org/ojs/index.php/ejssm/article/viewArticle/30/24].

Droegemeier, K. K., and R. B. Wilhelmson, 1985: Three-dimensional numerical modeling of convection produced by interacting thunderstorm outflows. Part I: Control simulation and low-level moisture variations. *J. Atmos. Sci.*, **42**, 2381–2403, doi:10.1175/1520-0469(1985)042⟨2381:TDNMOC⟩2.0.CO;2.

Dubois, J. A., and P. L. Spencer, 2005: Computing divergence from a surface network: Comparison of the triangle and pentagon methods. *Wea. Forecasting*, **20**, 596–608, doi:10.1175/WAF867.1.

Emmel, C., P. Knippertz, and O. Schulz, 2010: Climatology of convective density currents in the southern foothills of the Atlas Mountains. *J. Geophys. Res.*, **115**, D11 115, doi:10.1029/2009JD012863.

Engerer, N. A., D. J. Stensrud, and M. C. Coniglio, 2008: Surface characteristics of cold pools. *Mon. Wea. Rev.*, **136**, 4839–4849, doi:10.1175/2008MWR2528.1.

Feng, Z., S. Hagos, A. Rowe, C. Burleyson, M. Martini, and S. deSzoeke, 2015: Mechanisms of convective cloud organization by cold pools over tropical warm ocean during the AMIE/DYNAMO field campaign. *J. Adv. Model. Earth Syst.*, **7**, 357–381, doi:10.1002/2014MS000384.

Fujita, T., 1955: Results of detailed synoptic studies of squall lines. *Tellus*, **7**, 405–436, doi: 10.3402/tellusa.v7i4.8920.

Fujita, T., 1959: Precipitation and cold air production in mesoscale thunderstorm systems. *J. Meteor.*, **16**, 454–466, doi:10.1175/1520-0469(1959)016⟨0454:PACAPI⟩2.0.CO;2.

Fujita, T. T., and R. M. Wakimoto, 1981: Five scales of airflow associated with a series of downbursts on 16 July 1980. *Mon. Wea. Rev.*, **109**, 1438–1456, doi:10.1175/1520-0493(1981)109⟨1438:FSOAAW⟩2.0.CO;2.

Hocker, J. E., and J. B. Basara, 2008a: A 10-year spatial climatology of squall line storms across Oklahoma. *Int. J. Climatol.*, **28**, 765–775, doi:10.1002/joc.1579.

Hocker, J. E., and J. B. Basara, 2008b: A geographic information systems-based analysis of supercells across Oklahoma from 1994 to 2003. *J. Appl. Meteor. Climatol.*, **47**, 1518–1538, doi: 10.1175/2007JAMC1673.1.

Humphreys, W. J., 1914: The thunderstorm and its phenomena. *Mon. Wea. Rev.*, **42**, 348–380, doi:10.1175/1520-0493(1914)42⟨348:TTAIP⟩2.0.CO;2.

Johnson, R. H., 1976: The role of convective-scale precipitation downdrafts in cumulus and synoptic-scale interactions. *J. Atmos. Sci.*, **33**, 1890–1910, doi:10.1175/1520-0469(1976)033⟨1890:TROCSP⟩2.0.CO;2.

Johnson, R. H., and M. E. Nicholls, 1983: A composite analysis of the boundary layer accompanying a tropical squall line. *Mon. Wea. Rev.*, **111**, 308–319, doi:10.1175/1520-0493(1983)111⟨0308:ACAOTB⟩2.0.CO;2.

Kain, J. S., and J. M. Fritsch, 1990: A one-dimensional entraining/detraining plume model and its application in convective parameterization. *J. Atmos. Sci.*, **47**, 2784–2802, doi:10.1175/1520-0469(1990)047⟨2784:AODEPM⟩2.0.CO;2.

Knippertz, P., J. Trentmann, and A. Seifert, 2009: High-resolution simulations of convective cold pools over the northwestern Sahara. *J. Geophys. Res.*, **114**, D08 110, doi:10.1029/2008JD011271.

Knupp, K., and W. Cotton, 1985: Convective cloud downdraft structure: An interpretive survey. *Rev. Geophys.*, **23**, 183–215, doi:10.1029/RG023i002p00183.

Li, Z., P. Zuidema, and P. Zhu, 2014: Simulated convective invigoration processes at trade-wind cumulus cold pool boundaries. *J. Atmos. Sci.*, **71**, 2823–2841, doi:10.1175/JAS-D-13-0184.1.

Mapes, B. E., and R. Neale, 2011: Parameterizing convective organization to escape the entrainment dilemma. *J. Adv. Model. Earth Syst.*, **3**, M06 004, doi:10.1029/2011MS000042.

McPherson, R. A., and Coauthors, 2007: Statewide monitoring of the mesoscale environment: A technical update on the Oklahoma Mesonet. *J. Atmos. Oceanic Technol.*, **24**, 301–321, doi:10.1175/JTECH1976.1.

Moorthi, S., and M. J. Suarez, 1992: Relaxed Arakawa-Schubert: A parameterization of moist convection for general circulation models. *Mon. Wea. Rev.*, **120**, 978–1002, doi:10.1175/1520-0493(1992)120⟨0978:RASAPO⟩2.0.CO;2.

Newton, C. W., 1950: Structure and mechanism of the prefrontal squall line. *J. Meteor.*, **7**, 210–222, doi:10.1175/1520-0469(1950)007⟨0210:SAMOTP⟩2.0.CO;2.

Nicholls, M. E., and R. H. Johnson, 1984: A model of a tropical squall line boundary layer wake. *J. Atmos. Sci.*, **41**, 2774–2792, doi:10.1175/1520-0469(1984)041⟨2774:AMOATS⟩2.0.CO;2.

Pan, D.-M., and D. A. Randall, 1998: A cumulus parameterization with a prognostic closure. *Quart. J. Roy. Meteor. Soc.*, **124**, 949–981, doi:10.1002/qj.49712454714.

Qian, Y., G. S. Young, and W. M. Frank, 1998: A convective wake parameterization scheme for use in general circulation models. *Mon. Wea. Rev.*, **126**, 456–469, doi:10.1175/1520-0493(1998)126⟨0456:ACWPSF⟩2.0.CO;2.

Redl, R., A. H. Fink, and P. Knippertz, 2015: An objective detection method for convective cold pool events and its application to Northern Africa. *Mon. Wea. Rev.*, **143**, 5055–5072, doi:10.1175/MWR-D-15-0223.1.

Rotunno, R., J. B. Klemp, and M. L. Weisman, 1988: A theory for strong, long-lived squall lines. *J. Atmos. Sci.*, **45**, 463–485, doi:10.1175/1520-0469(1988)045⟨0463:ATFSLL⟩2.0.CO;2.

Rozbicki, J. J., G. S. Young, and Y. Qian, 1999: Test of a convective wake parameterization in the single-column version of CCM3. *Mon. Wea. Rev.*, **127**, 1347–1361, doi:10.1175/1520-0493(1999)127⟨1347:TOACWP⟩2.0.CO;2.

Sanders, F., 1955: An investigation of the structure and dynamics of an intense surface frontal zone. *J. Meteor.*, **12**, 542–552, doi:10.1175/1520-0469(1955)012⟨0542:AIOTSA⟩2.0.CO;2.

Schultz, D. M., 2004: Cold fronts with and without prefrontal wind shifts in the central United States. *Mon. Wea. Rev.*, **132**, 2040–2053, doi:10.1175/1520-0493(2004)132⟨2040:CFWAWP⟩2.0.CO;2.

Schultz, D. M., 2005: A review of cold fronts with prefrontal troughs and wind shifts. *Mon. Wea. Rev.*, **133**, 2449–2472, doi:10.1175/MWR2987.1.

Schultz, D. M., 2008: Perspectives on Fred Sanders' research on cold fronts. *Synoptic-Dynamic Meteorology and Weather Analysis and Forecasting: A Tribute to Fred Sanders.*, Vol. 55, Amer. Meteor. Soc., 109–126, doi:10.1175/0065-9401-33.55.109.

Schultz, D. M., and P. J. Roebber, 2008: The fiftieth anniversary of Sanders (1955): A mesoscale model simulation of the cold front of 17-18 April 1953. *Synoptic-Dynamic Meteorology and Weather Analysis and Forecasting: A Tribute to Fred Sanders.*, Vol. 55, Amer. Meteor. Soc., 127–143, doi:10.1175/0065-9401-33.55.127.

Schultz, D. M., and W. J. Steenburgh, 1999: The formation of a forward-tilting cold front with multiple cloud bands during Superstorm 1993. *Mon. Wea. Rev.*, **127**, 1108–1124, doi:10.1175/1520-0493(1999)127⟨1108:TFOAFT⟩2.0.CO;2.

Seigel, R. B., and S. C. van den Heever, 2012: Simulated density currents beneath embedded stratified layers. *J. Atmos. Sci.*, **69**, 2192–2200, doi:10.1175/JAS-D-11-0255.1.

Stensrud, D. J., G. S. Manikin, E. Rogers, and K. E. Mitchell, 1999: Importance of cold pools to NCEP mesoscale Eta model forecasts. *Wea. Forecasting*, **14**, 650–670, doi:10.1175/1520-0434(1999)014⟨0650:IOCPTN⟩2.0.CO;2.

Stout, G. E., R. H. Blackmer Jr., J. B. Holleyman, and H. M. Gibson, 1957: Mesometeorological analysis of atmospheric phenomena. Tech. rep., Quart. Tech. Rep. Nos. 1-10, Illinois State Water Survey, 112 pp. doi:http://www.isws.illinois.edu/pubdoc/cr/iswscr-14.pdf.

Sun, R., and S. K. Krueger, 2012: Mesoanalysis of the interactions of precipitating convection and the boundary layer. *J. Adv. Model. Earth Syst.*, **4**, M04 004, doi:10.1029/2011MS000096.

Tepper, M., 1950: A proposed mechanism of squall lines: The pressure jump line. *J. Meteor.*, **7**, 21–29, doi:10.1175/1520-0469(1950)007⟨0021:APMOSL⟩2.0.CO;2.

Tompkins, A. M., 2001: Organization of tropical convection in low vertical wind shears: The role of cold pools. *J. Atmos. Sci.*, **58**, 1650–1672, doi:10.1175/1520-0469(2001)058⟨1650:OOTCIL⟩2.0.CO;2.

Wakimoto, R. M., 1982: The life cycle of thunderstorm gust fronts as viewed with Doppler radar and rawinsonde data. *Mon. Wea. Rev.*, **110**, 1060–1082, doi:10.1175/1520-0493(1982)110⟨1060:TLCOTG⟩2.0.CO;2.

LIST OF FIGURES

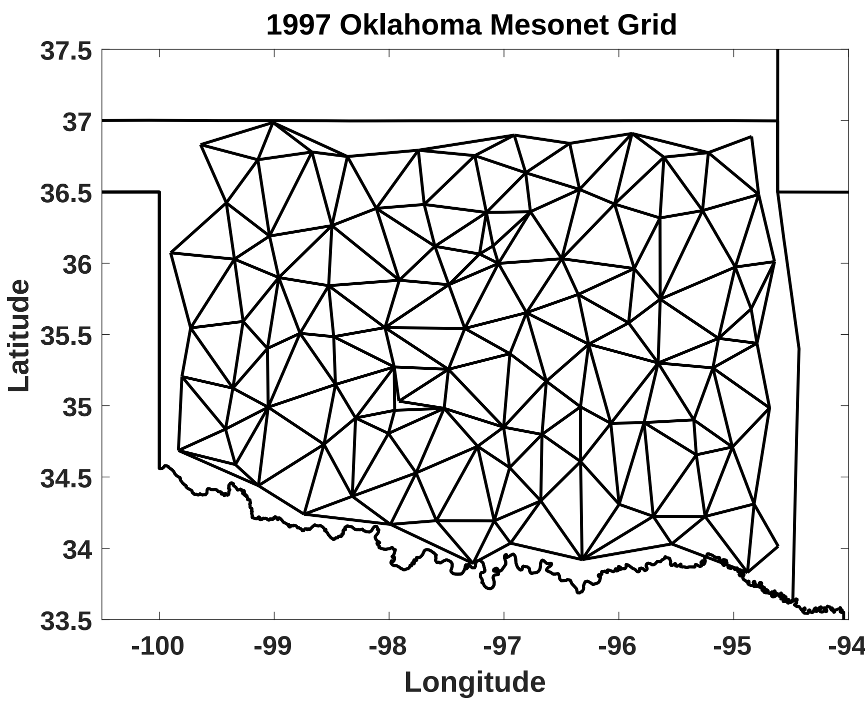

FIG. 1. Map of the Oklahoma Mesonet grid used for 1997. Delaunay triangulation was used to connect the stations to form the grid. This map shows the triangles which remain after the low aspect ratio triangles were removed. The removed triangles are the gaps around the outside of the grid and a small low aspect ratio area near 35°N 98°W.

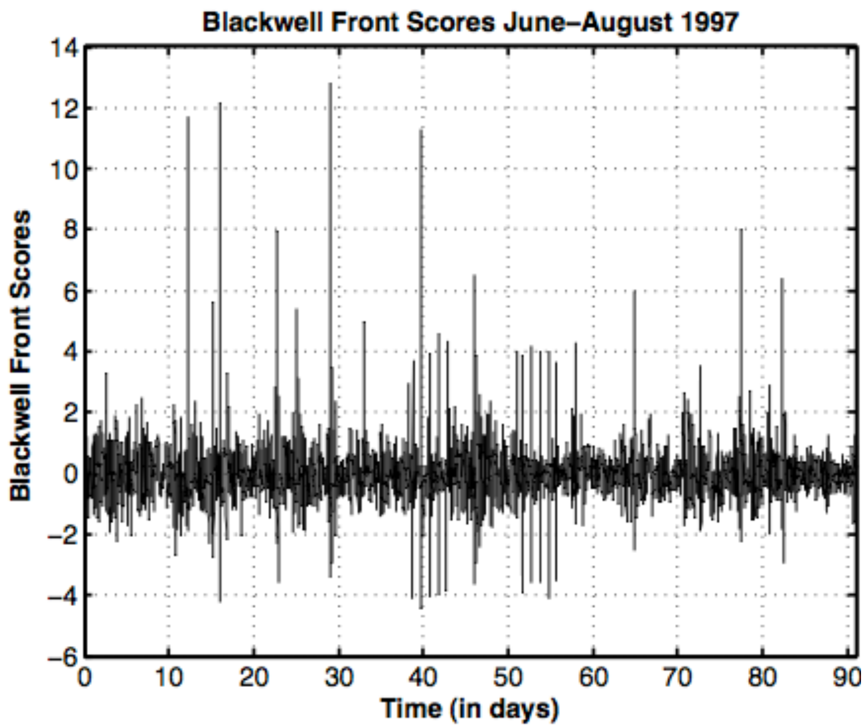

FIG. 2. Front scores for the JJA 1997 period at the Blackwell Mesonet station (36.75°N, 97.25°W). Large positive front scores indicate frontal passages.

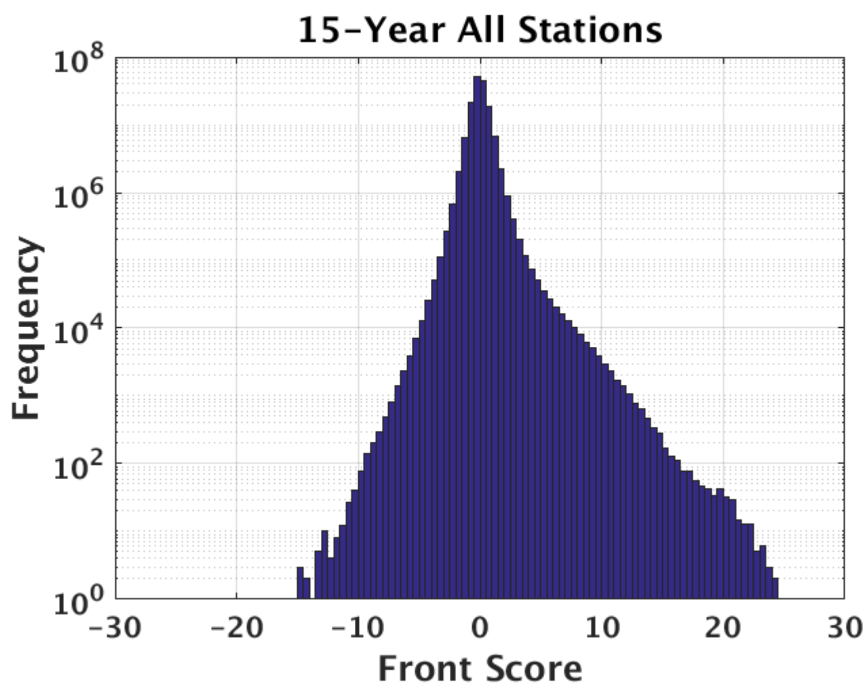

FIG. 3. Front score frequency for all stations at each 5-minute observation over the 1997-2011 period.

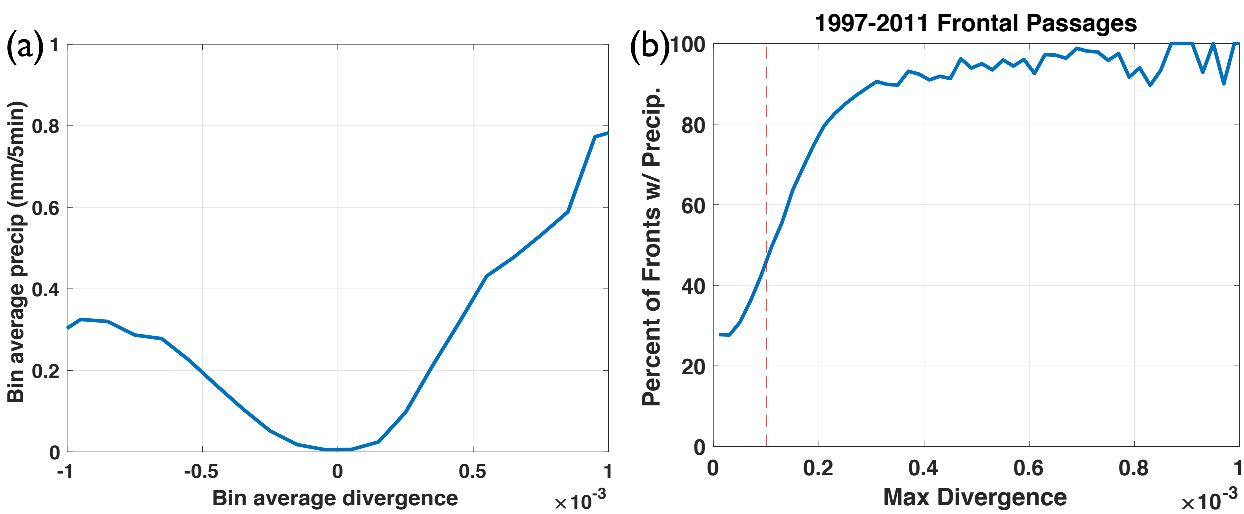

839 FIG. 4. The (a) average surface precipitation (in mm 5min^{-1}) for each divergence bin and (b) percentage of frontal passages which occurred with surface precipitation, as a function of maximum divergence associated with the front.

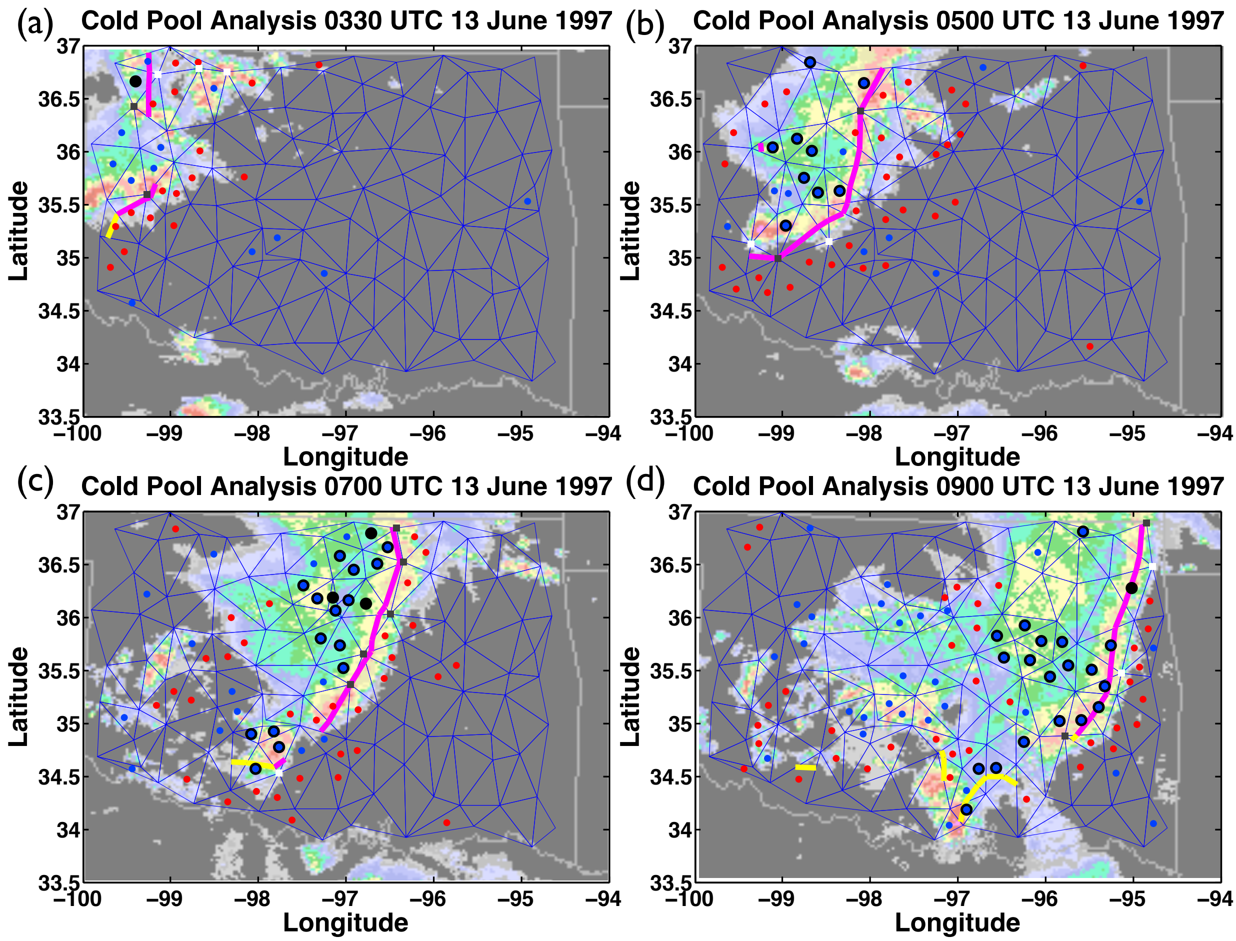

FIG. 5. Front and cold pool analysis for 13 June 1997 (a) 0330 UTC, (b) 0500 UTC, (c) 0700 UTC, and (d) 0900 UTC. Red dots are $D_i < -10^{-4}\mathrm{s}^{-1}$ while blue dots are $D_i > 10^{-4}\mathrm{s}^{-1}$. Yellow lines are frontal passages with FSs of $3 <= \mathrm{FS} < 5$ while magenta lines are frontal passages with FSs of 5+. White squares are stations where at the current timestep the FS is $3 <= \mathrm{FS} < 5$; gray squares designate stations currently with FSs at 5+. Black dots indicate triangles currently designated as cold pools. Radar images are from the UCAR image archive. http://www2.mmm.ucar.edu/imagearchive/

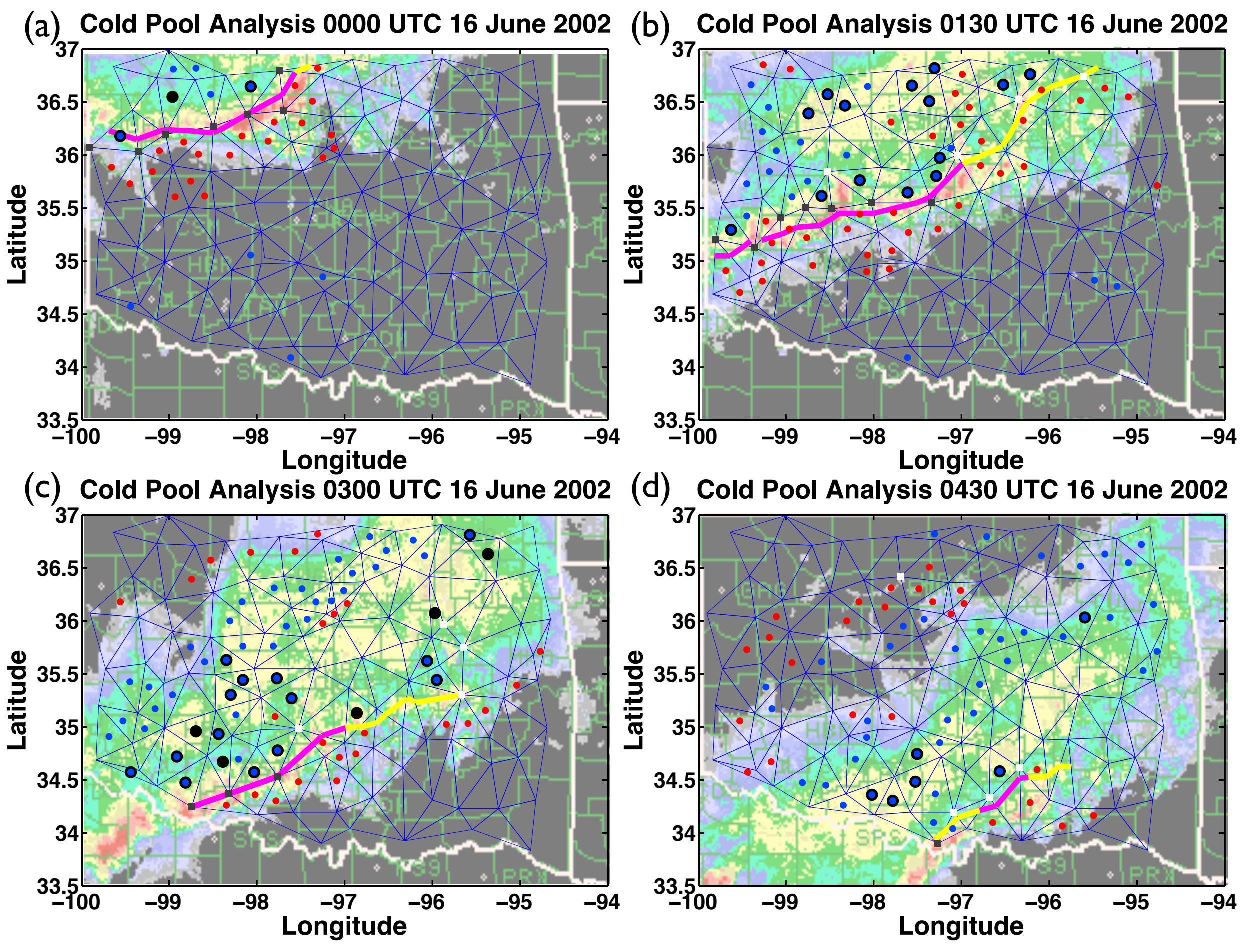

848 FIG. 6. Same as Figure 5 except for 16 June 2002 (a) 0000 UTC, (b) 0130 UTC, (c) 0300 UTC, and (d) 0430
849 UTC.

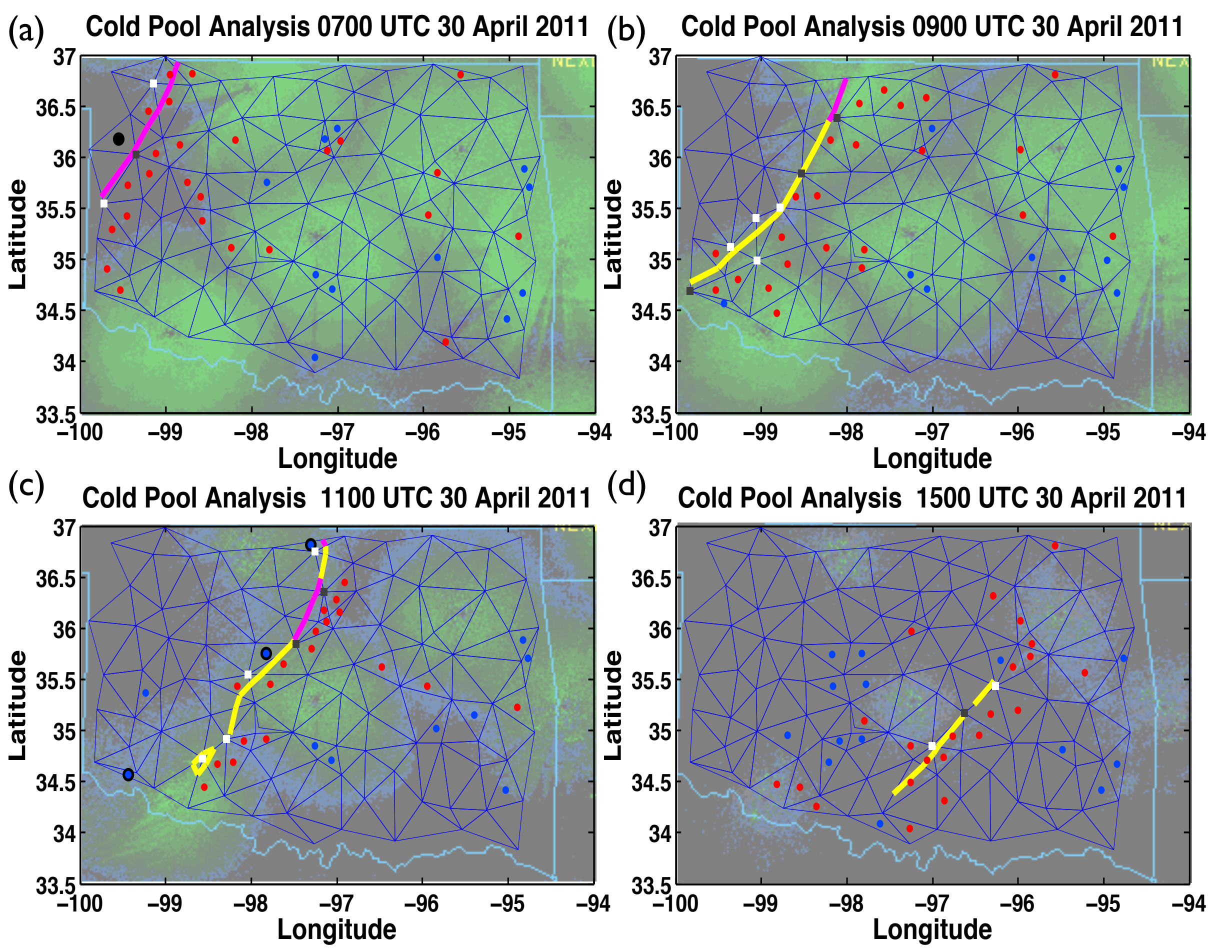

FIG. 7. Same as Figure 5 except for 30 April 2011 (a) 0700 UTC, (b) 0900 UTC, (c) 1100 UTC, and (d) 1500 UTC.

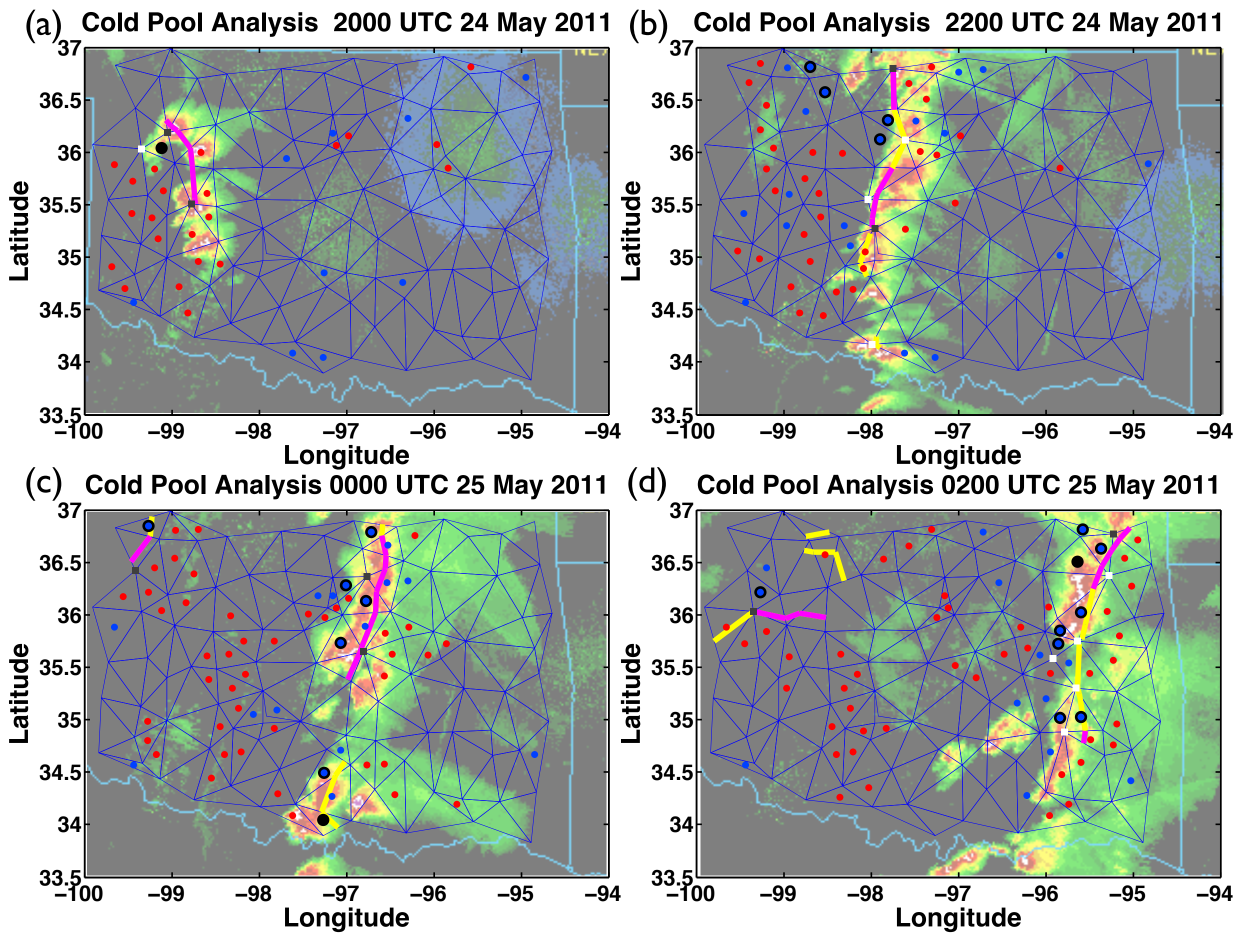

852 FIG. 8. Same as Figure 5 except for 24 May 2011 (a) 2000 UTC, (b) 2200 UTC, 25 May 2011 (c) 0000 UTC,
853 and (d) 0200 UTC.

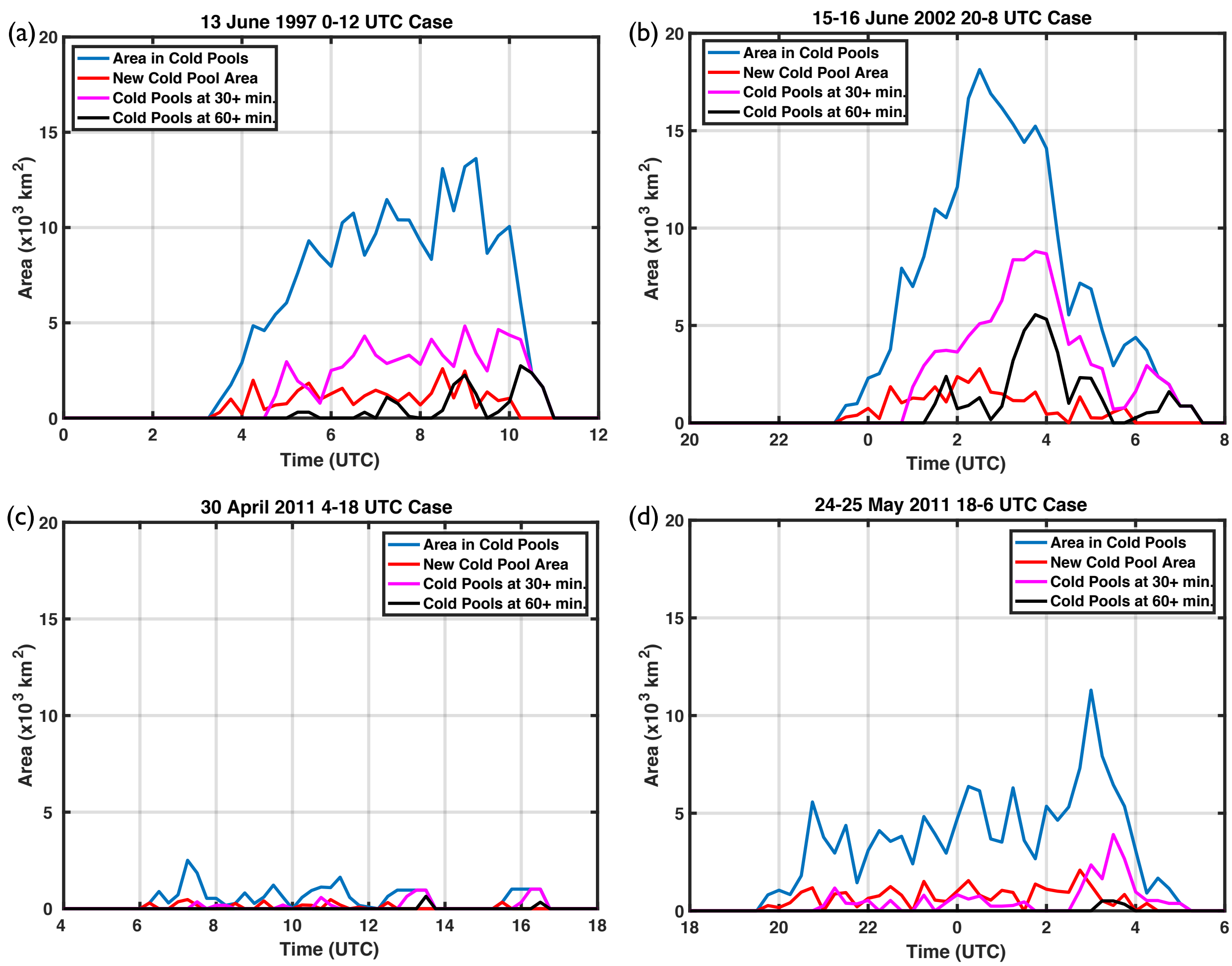

FIG. 9. Cold pool areas for the case studies: a) 13 June 1997 0-12 UTC, b) 15-16 June 2002 20-8 UTC, c) 30 April 4-18 UTC, d) 24-25 May 2011 18-6 UTC. Cold pool areas are shown as 15-min averages for total area in cold pools (blue), new cold pool area (red), area residing in a cold pool at least 30 mins (magenta), and area residing in a cold pool at least 60 mins (black).

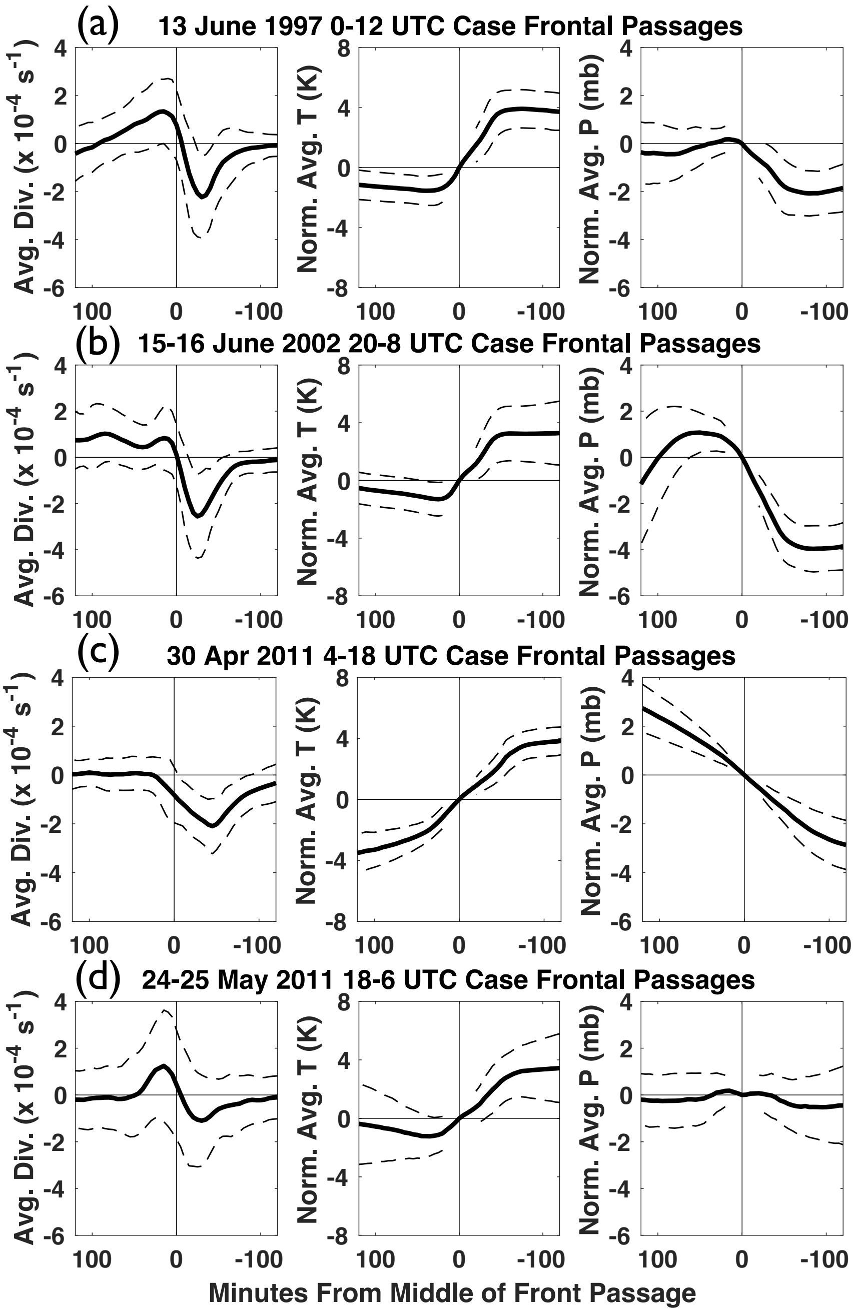

858 FIG. 10. Average (solid) and +- 1 standard deviation (dashed) divergence, normalized temperature, and normalized pressure values for frontal passages at Mesonet triangles. The x-axis is reversed to show a west to east pattern. Case studies are: a) 13 June 1997 0-12 UTC, b) 15-16 June 2002 20-8 UTC, c) 30 April 4-18 UTC, d) 24-25 May 2011 18-6 UTC.

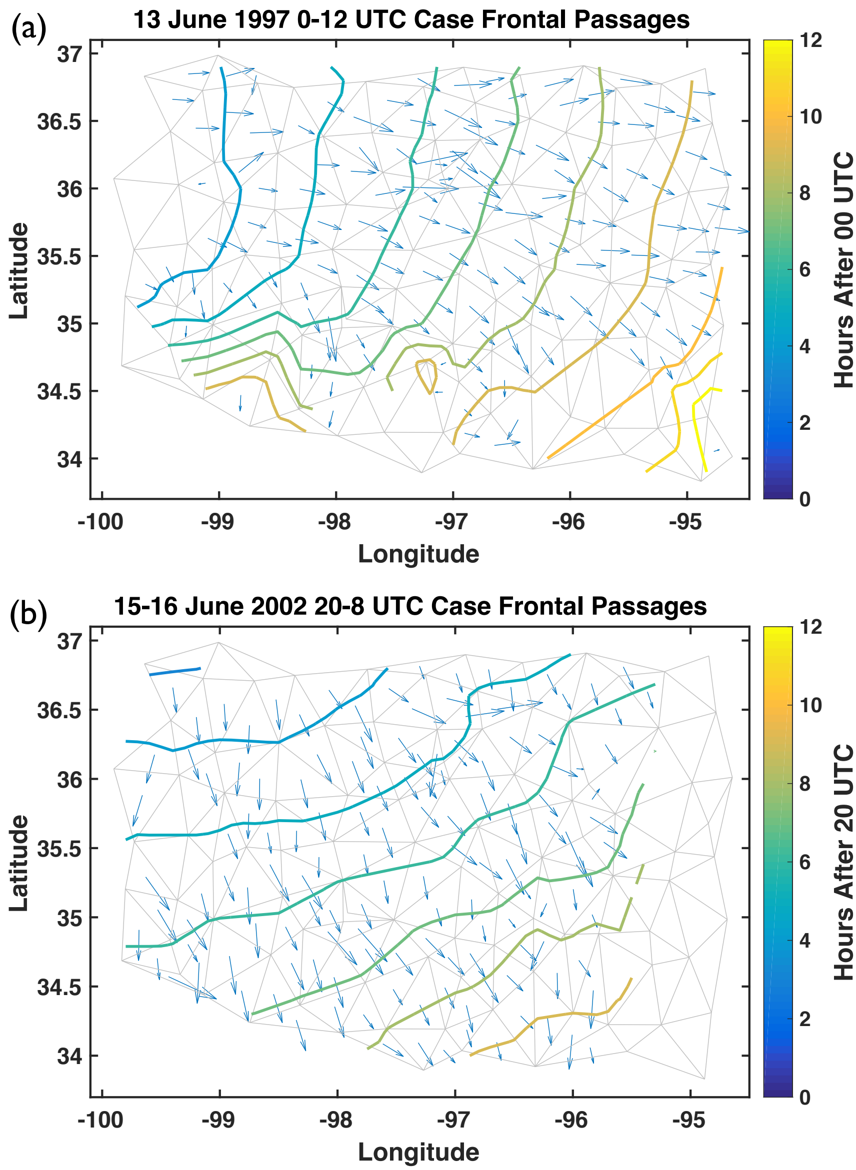

FIG. 11. Frontal passage location and timing (contours) with front speeds (in m s^{-1}) represented by quivers. Case studies are: a) 13 June 1997 0-12 UTC and b) 15-16 June 2002 20-8 UTC.

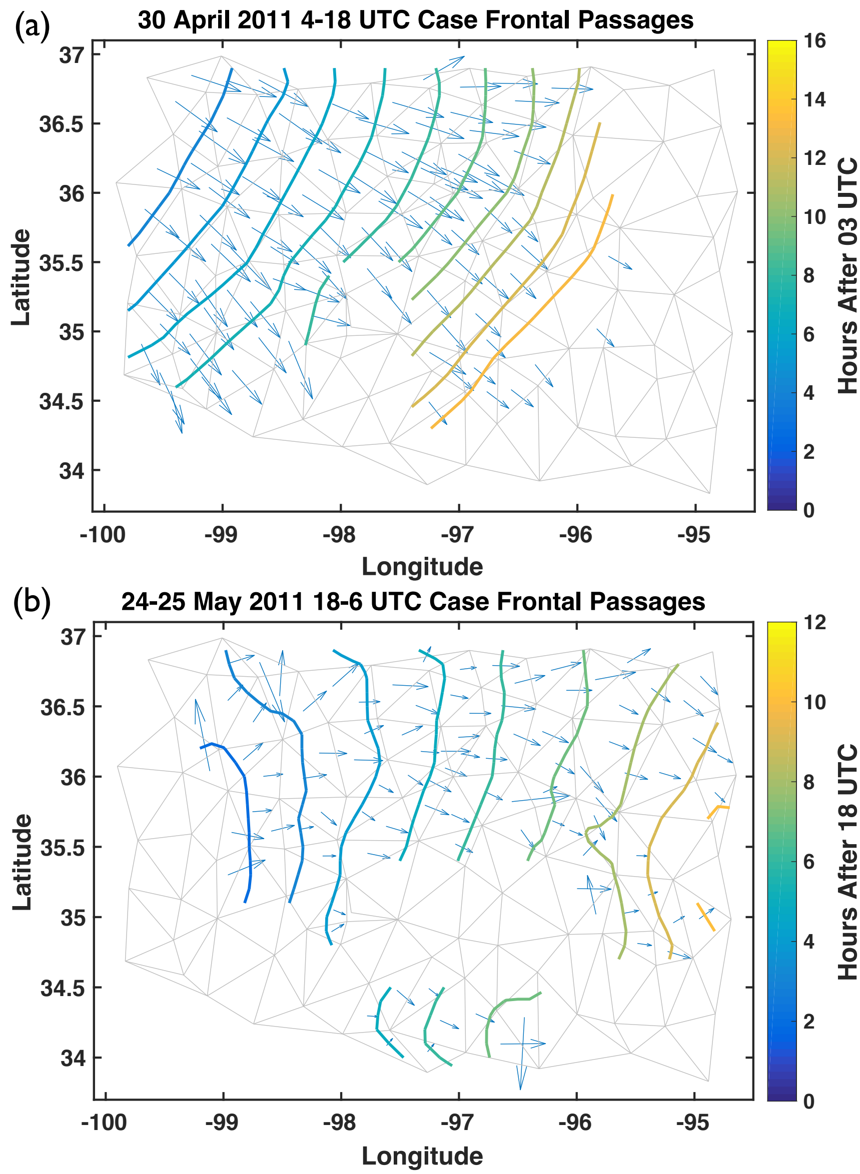

FIG. 12. Frontal passage location and timing (contours) with front speeds (in m s^{-1}) represented by quivers. Case studies are: a) 30 April 2011 4-18 UTC and b) 24-25 May 2011 18-6 UTC.

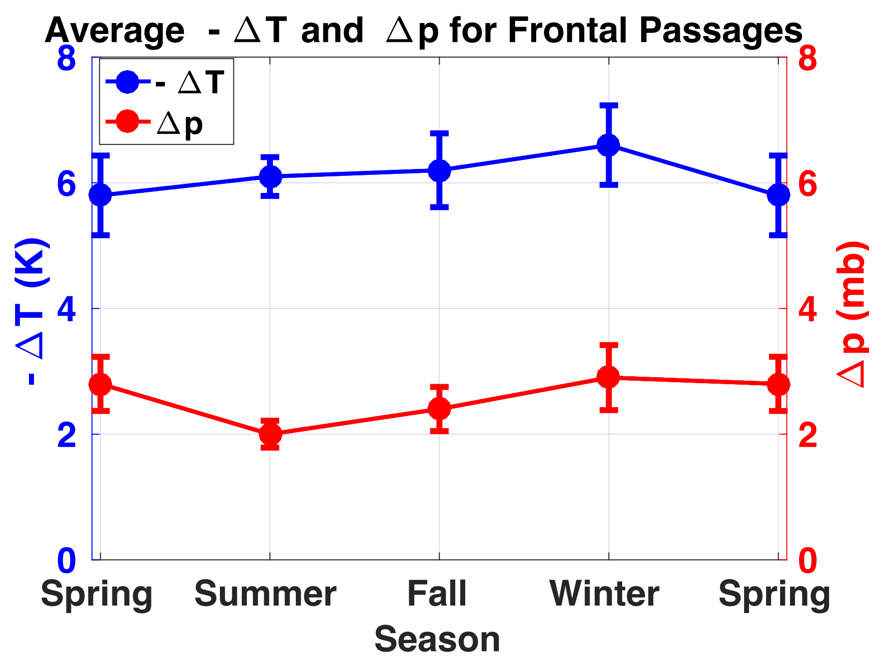

866 FIG. 13. Seasonal average $-\Delta T$ and Δp and standard deviations for 1997-2011 frontal passages. Seasons are
867 defined as: spring (MAM), summer (JJA), fall (SON), and winter (DJF). The number of fronts by season are:
868 23,811 in spring, 22,785 in summer, 13,009 in fall, and 12,539 in winter.

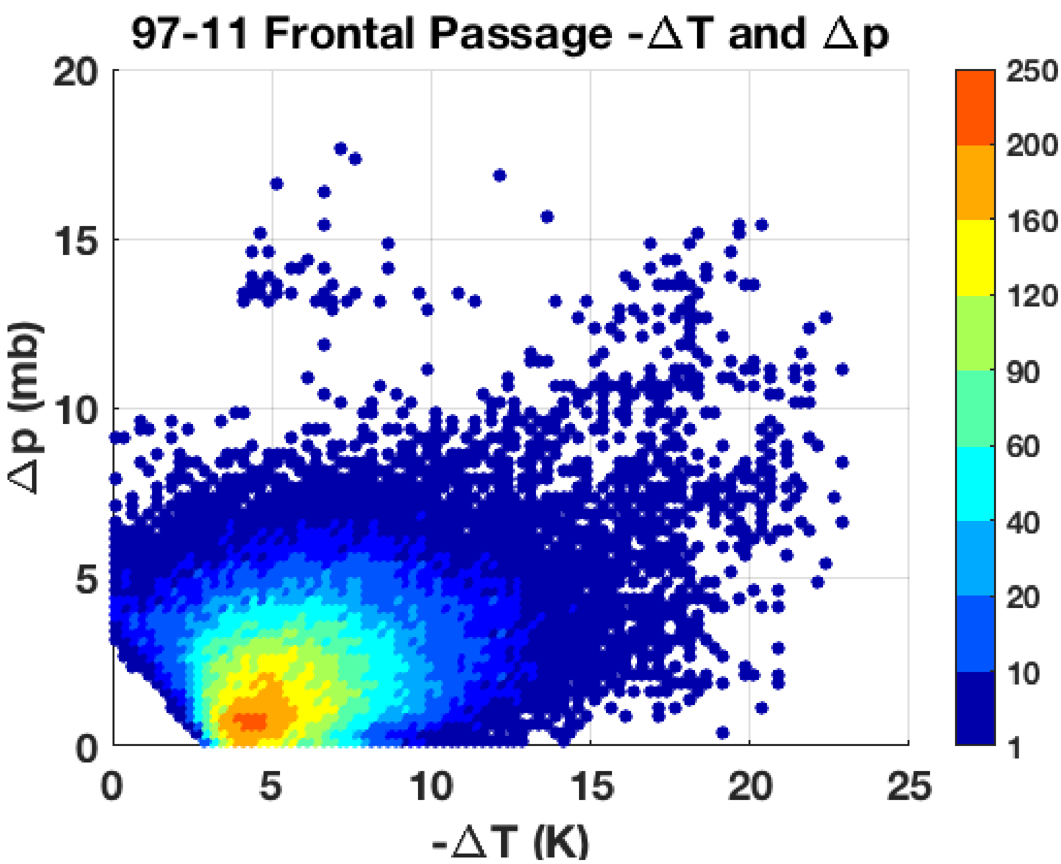

FIG. 14. Δp versus $-\Delta T$ at stations that are part of frontal passages across triangles in the Oklahoma Mesonet from the 1997-2011 period. The color bar represents the frequency of occurrence. Bin widths are .1 K and .1 mb. The correlation is 0.28.

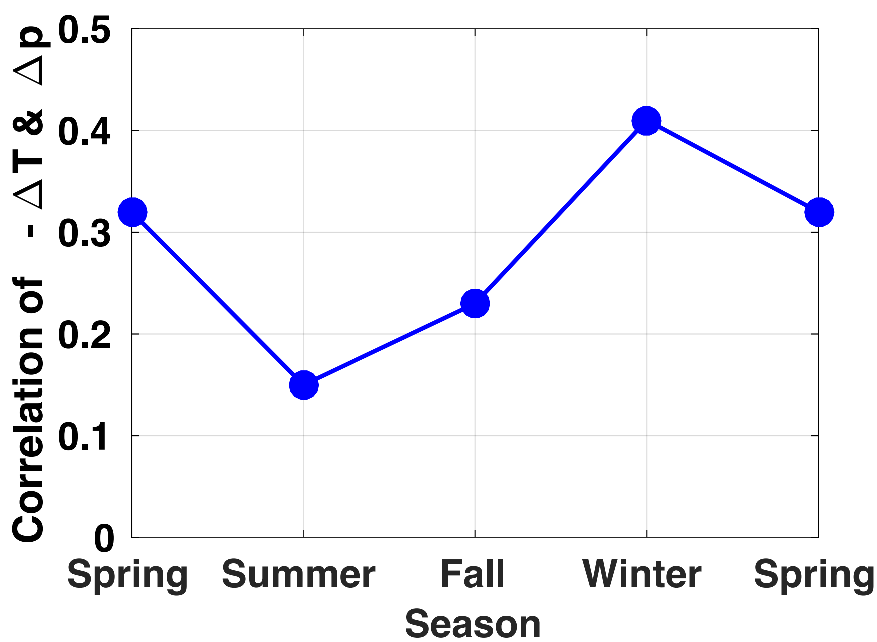

FIG. 15. Seasonal correlations between $-\Delta T$ and Δp at stations during frontal passages across triangles.

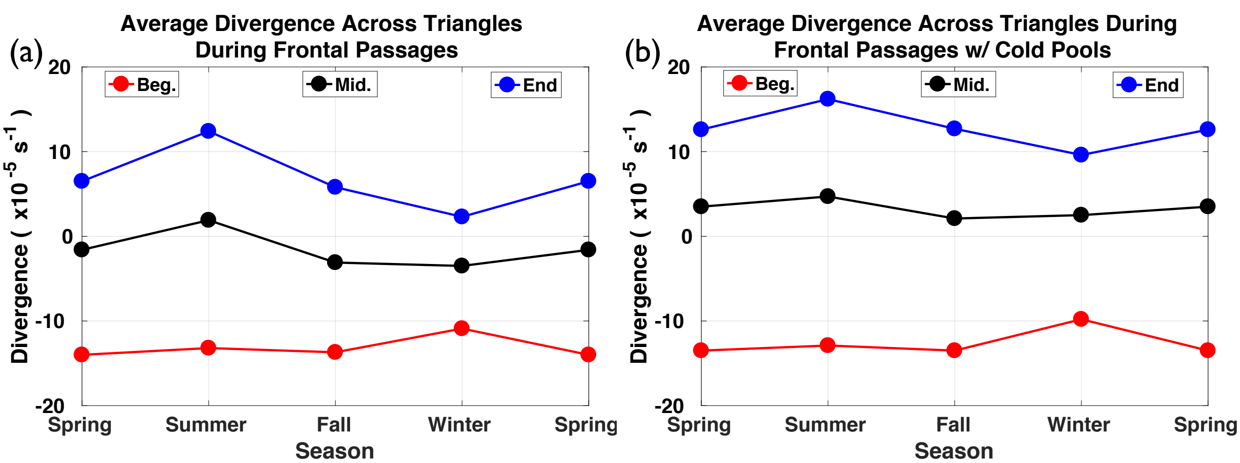

872 FIG. 16. Average divergence values (in $10^{-5}\mathrm{s}^{-1}$) at the beginning, middle, and end of (a) all frontal passages
873 and (b) frontal passages resulting in cold pools experienced by Mesonet triangles from 1997-2011 by season.

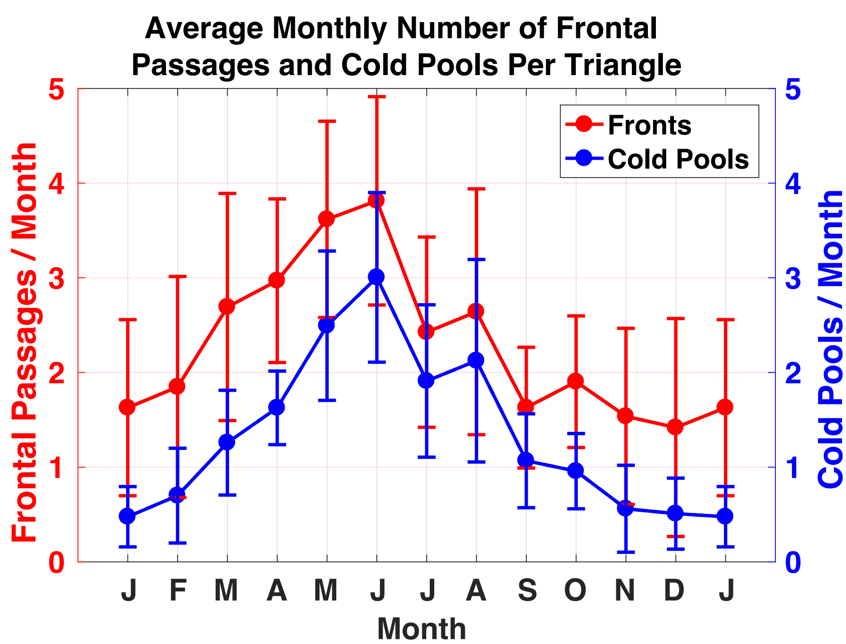

FIG. 17. Average and standard deviation of the number of fronts and cold pools experienced by Mesonet triangles per month for the 1997-2011 period.

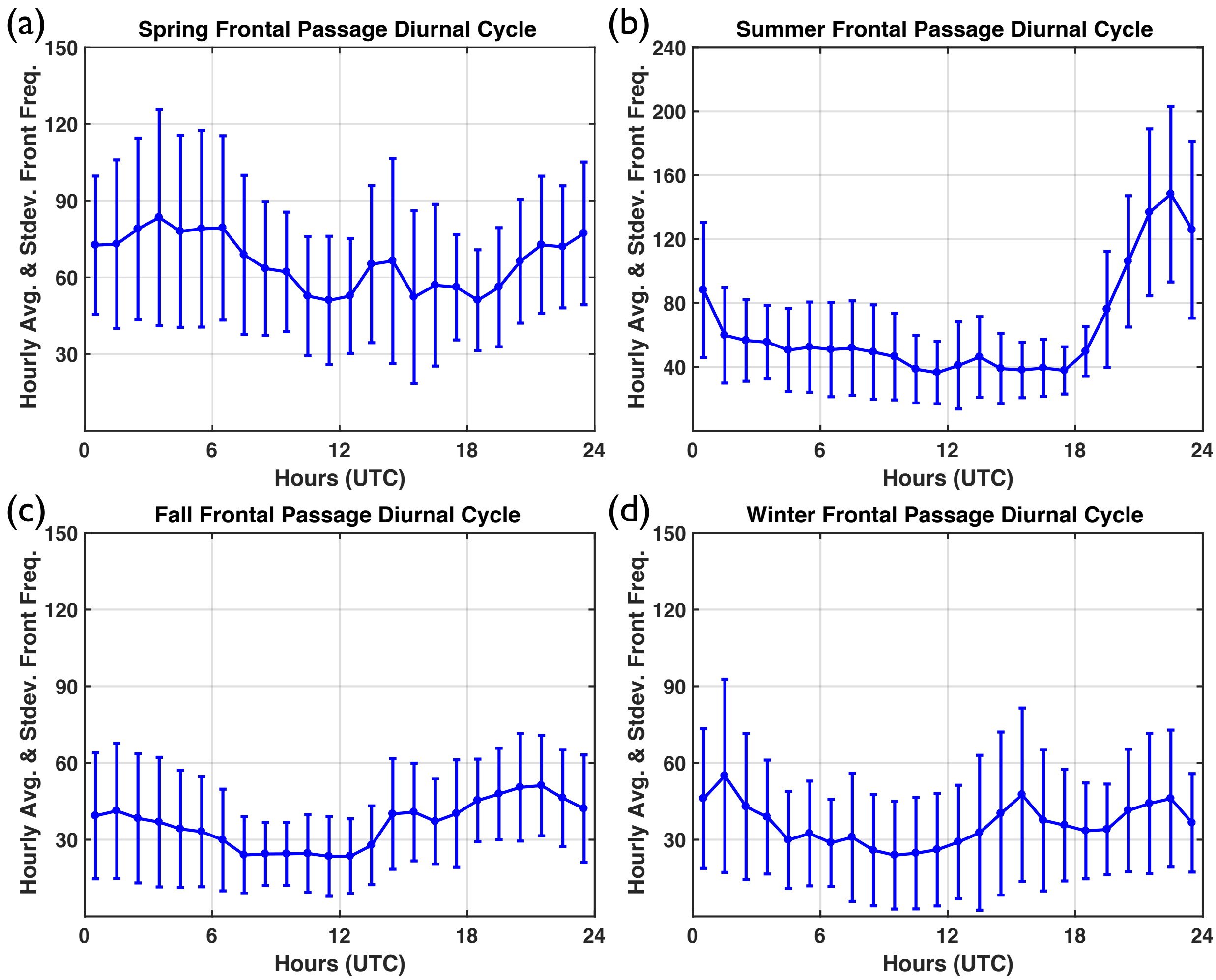

FIG. 18. Seasonally averaged (MAM, JJA, SON, DJF) diurnal cycle (in UTC time) and standard deviations of frontal passage frequency at triangles in the Oklahoma Mesonet for the 1997-2011 period.

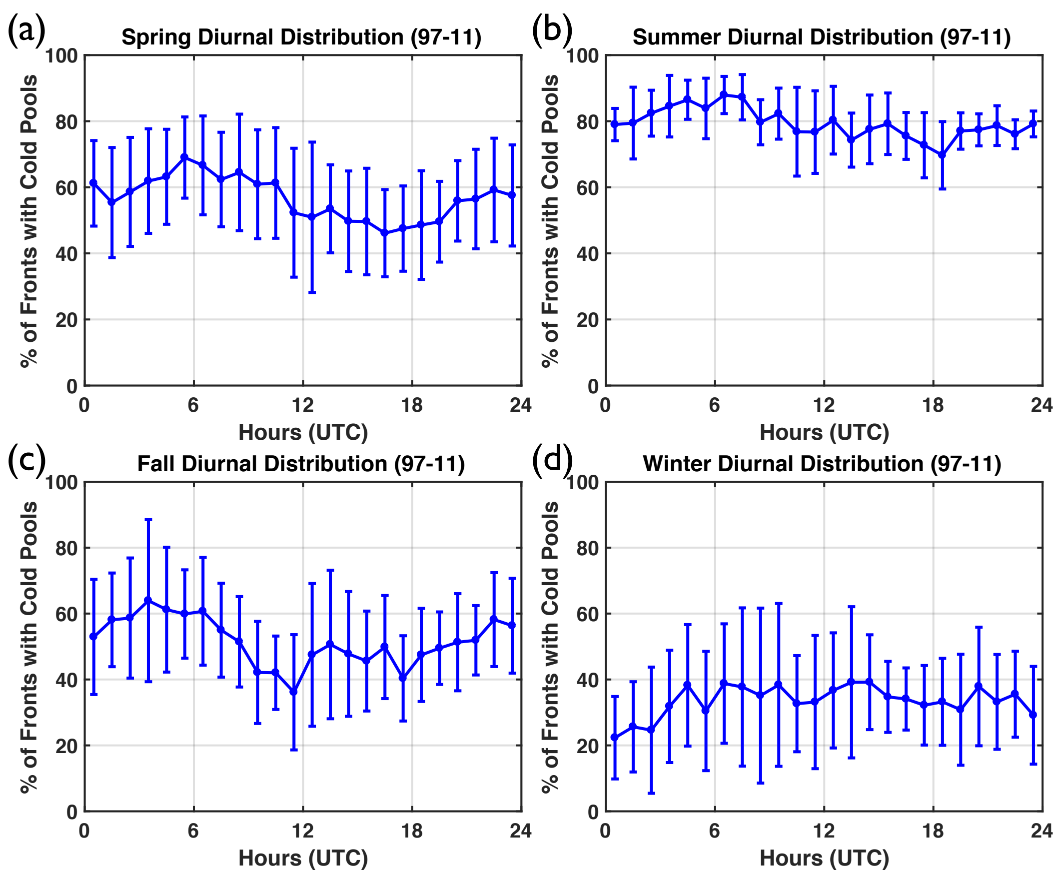

FIG. 19. Seasonally averaged diurnal cycle (in UTC time) and standard deviations of the percentage of frontal passages resulting in cold pools for the 1997-2011 period.